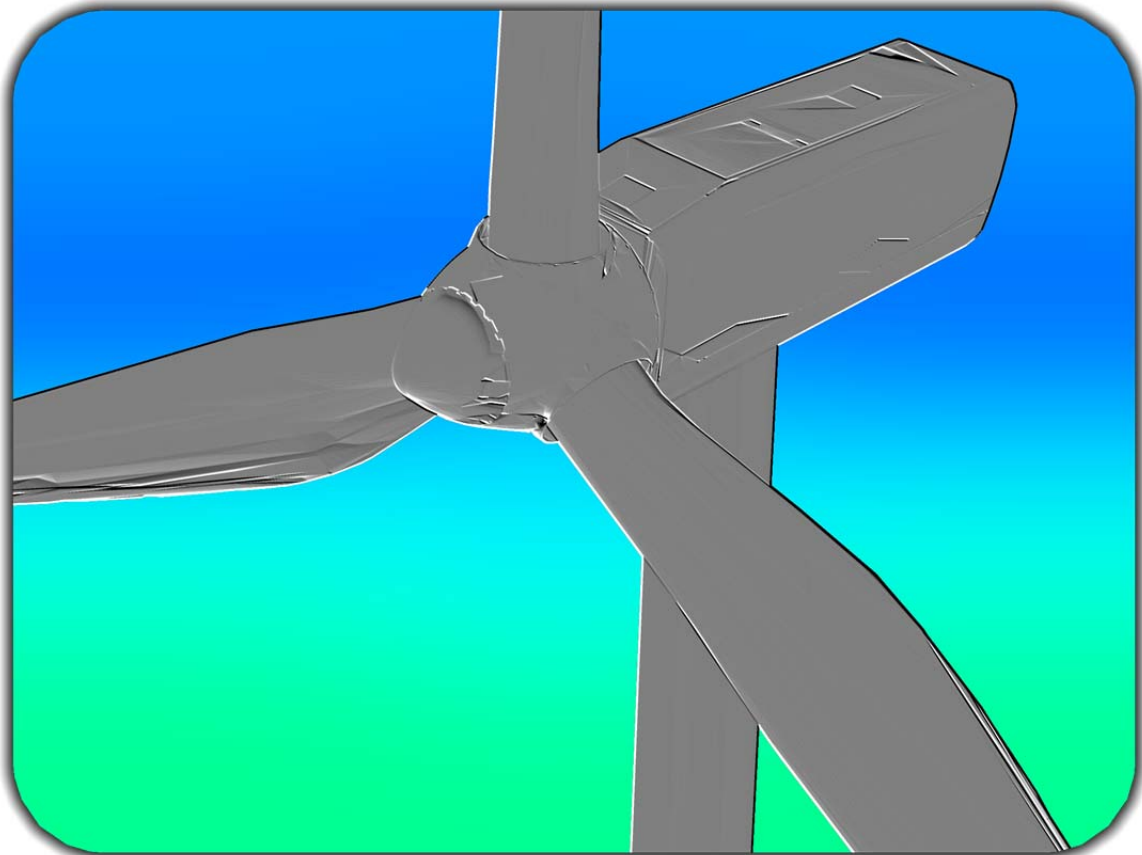


# CHALMERS



## Design of Experiments and Analysis for Drive Train Test Rig

*Master's Thesis in the International Master's Programme in Applied Mechanics*

**STEPHEN GABRIEL MCCANN**

Department of Applied Mechanics  
*Division of Dynamics*  
CHALMERS UNIVERSITY OF TECHNOLOGY  
Göteborg, Sweden 2013  
Master's thesis 2013:30



MASTER'S THESIS IN INTERNATIONAL MASTER'S PROGRAMME IN  
APPLIED MECHANICS

Design of Experiments and Analysis for  
Drive Train Test Rig

STEPHEN GABRIEL MCCANN

Department of Applied Mechanics  
*Division of Dynamics*  
CHALMERS UNIVERSITY OF TECHNOLOGY  
Göteborg, Sweden 2013

**Design of Experiments and Analysis for Drive Train Test Rig**

STEPHEN GABRIEL MCCANN

© STEPHEN GABRIEL MCCANN, 2013

Master's Thesis 2013:30

ISSN 1652-8557

Department of Applied Mechanics

Division of Dynamics

Chalmers University of Technology

SE-412 96 Göteborg

Sweden

Telephone: + 46 (0)31-772 1000

Chalmers Reproservice  
Göteborg, Sweden 2013

To my dearly departed mother, Eleanor Frances Powell, for never giving up on me.



## **Design of Experiments and Analysis for Drive Train Test**

Master's Thesis in the International Master's Program in Applied Mechanics

STEPHEN GABRIEL MCCANN

Department of Applied Mechanics

Division of Dynamics

Chalmers University of Technology

### ABSTRACT

Green energy initiatives and carbon reduction schemes are central to policymakers globally. The existing fleet of indirect drive, gearbox driven wind turbines are under scrutiny in regards to their stated feasibility and longevity. At the time of writing, design standards and reliability studies of wind turbines is to be considered an immature area of study. Advanced vibration study as a basis for reliability is being undertaken by industry, governments and academia. Chalmers University of Technology has developed a test rig which is a modular and upgradeable scaled down model of a direct drive wind turbine. Concepts for the test rig were developed through study of existing test facilities with the US Government's National Renewable Energy Laboratories and Hansen® transmissions various proving facilities. Development of the test rig involved established design techniques with the development of engineering, mathematical, and computational models. Test rig components were selected using scaling factors, usability and operability requirements, and through advice of both industry and experienced personnel within Chalmers. ABB® frequency controllers and motors fitted with sensors serve as the prime movers. Properties of the test rig were developed and analysed through use of stress analysis, dynamic modelling, and engineering drawings created with AutoCad®, with simulations completed through utilisation of Matlab®. Studies into the rotor shaft dynamics, torsional misalignments, bearing forces can be completed by implementation of strain gauges, non-contact displacement sensors, shaft rotation and speed encoders, as well as ABB® torque sensing circuitry. Design and implementation of this test rig allows for basic and advanced study of dynamics suitable to both undergraduate laboratory and post doctoral researcher, for mechanical and electrical engineers. Further studies and development will be carried out by Chalmers staff and researchers.

Key words: drive train dynamics, EMC modelling, test rig, vibration, wind turbine



## Preface

Thorough understanding of failure mechanisms is vital to ensure long term success to the wind turbine industry. This report details the design and verification process for a wind turbine drive train test rig, which is an upgradeable and modular construction allowing for various real time dynamic simulations, analogous to a functional wind turbine drive train. The report and test rig are part of the ongoing research into wind turbine reliability supported by the Swedish Wind Power Technology Centre [<http://www.chalmers.se/ee/swptc-en>]. This five month study has culminated in the initial construction of what will be one of Chalmers University of Technology's future test apparatus, located in the Vibrations and Smart Structures Laboratory of the Division of Dynamics.

An initial concept was realised through past studies at Chalmers University of Technology which served as the basis for the proposed design project. Various academic and industrial research projects were examined to set the boundaries for the design. These concepts were then brought forward to a working physical model through use of traditional engineering design techniques. The design process and build required input from many people, including senior Chalmers staff and researchers, as well as outside fabricators and industry partnerships.

Chalmers staff welcomes and supports ERASMUS students inside their great institution, with a strong sense of team, professionalism, and open learning environment. A special thank you and appreciation goes out to my supervisors, Professor Dr. Viktor Berbyuk and Lecturer Dr. Håkan Johansson for their mentoring and continuous support throughout the project. Additional thanks goes to Research Engineer Jan Möller whose experience and vision aided the design process greatly. Appreciation is given to my thesis opponent, Saeed Asadi, who helped with perspective on the project and for some very good questions during my final presentation at Chalmers. Gratitude and thanks is also given to ABB® for their contribution to the project, in the form of a donated pair of high quality motors and frequency controllers which will serve as the centrepiece to the test rig.

I would like to express my appreciation to my fellow colleagues during my visit to Chalmers; Geoffrey Geldhof, Juan Pablo Sanches de Lara Garcia, Ana Pastor, and Alexander Sehlström. We started our projects together, as strangers to one another, all with difficult and time intensive projects before us. Somehow we got through it all and still managed to explore the university and City of Gothenburg, during which time we became friends and had some great nights out. I miss you already and will remember my time in Sweden with fondness. Finally, I thank my partner for her patience in putting up with me being on such a long academic sequester.

Göteborg June 2013

Stephen Gabriel McCann



# Contents

ABSTRACT	I
PREFACE	III
CONTENTS	V
TABLE OF FIGURES	VII
LIST OF TABLES	IX
NOTATIONS	X
1 INTRODUCTION	1
1.1 Background	1
1.2 Objective	1
1.2.1 Engineering Model	2
1.2.2 Mathematical Model	3
1.2.3 Computational Model	3
1.3 Reliability	3
1.4 NREL Gearbox Reliability Collaborative	4
1.5 Hansen® Transmission Test Rig	5
1.6 Failure Modes	6
1.7 Motivation for Chalmers Test Rig	7
1.8 Coordinate System	8
1.9 Conceptual Design	10
1.10 Safety	11
1.11 General Assembly	11
1.12 3-Phase Induction Motor and Frequency Drive	13
Further Details on Components	14
1.13 System Block Diagram	14
1.13.1 Displacement Sensor Arrangement	16
1.14 Bearing Housing	17
1.14.1 Physical Arrangement	17
1.14.2 Bearing Housing Equivalent Mechanical Model	18
1.15 Test Rig Quasi-Static Model – Setup 1	20
1.16 Test Rig Dynamic Model – Setup 1	21
1.17 Rotor Out of Balance Forcing Function Dynamic Model	22
1.18 Coupling Dynamic Model	22
2 TEST SYSTEM 1 DIFFERENTIAL EQUATIONS OF MOTION	24
2.1 System Formulas	24

2.2	Dynamic Analysis	26
2.3	Initial Conditions	27
2.4	Semi-Inverse Dynamic Analysis	27
2.5	Eigenfrequencies and Mode Shapes	30
3	DETERMINATION OF ECCENTRIC MASS FOR SETUP 1	32
3.1	System Parameters	34
3.1.1	Rotor Shaft Characteristics	35
3.1.2	Evaluation of Bearing Housing Spring Deflection	36
3.2	Evaluation of Torsional Vibration	42
3.3	Simulation of Torsional Vibration	42
3.3.1	Coupling 1	43
3.3.2	Coupling 2	44
3.3.3	Torsional Vibration Simulations	45
4	FRAME DYNAMICS	46
4.1	Test Frame Dynamic Analysis	46
4.2	Test Frame Stress Analysis	48
4.3	Support Frame Dynamics	48
4.4	Support Frame Stress Analysis	49
5	RESULTS	50
6	CONCLUSIONS AND OUTLOOK	51
7	REFERENCES	53
	APPENDIX I - DRAWINGS	55

## Table of Figures

Figure 1: <i>cycle for engineering design</i> .....	2
Figure 2: <i>NREL dynamometer test bed schematic diagram</i> .....	4
Figure 3: <i>NREL dynamometer test facility, Colorado</i> .....	5
Figure 4: <i>Hansen® 13.2 MW test rig</i> .....	6
Figure 5: <i>coordinate system for wind turbine</i> .....	9
Figure 6: <i>proposed test bed design</i> .....	10
Figure 7: <i>complete test rig arrangement, one motor and one bearing housing</i> .....	12
Figure 8: <i>characteristic torque curve for ABB® M3BP-160 motor</i> .....	13
Figure 9: <i>ABB® motor and variable frequency drive controller</i> .....	14
Figure 10: <i>system block diagram for wind turbine test bed, measuring Y and Z axis</i> .....	15
Figure 11: <i>National Instruments® cDAQ-9178</i> .....	15
Figure 12: <i>arrangement of displacement sensors with data flow</i> .....	16
Figure 13: <i>arrangement of the bearing housing with displacement sensors</i> .....	17
Figure 14: <i>equivalent model of bearing housing and spring retention system</i> .....	18
Figure 15: <i>Lesjöfors™ spring specificatio</i> .....	19
Figure 16: <i>static model of the test rig, complete, setup 1</i> .....	20
Figure 17: <i>dynamic model of test rig with rotor shaft angle, setup 1</i> .....	21
Figure 18: <i>eccentric mass setup for test rig inertia load case</i> .....	22
Figure 19: <i>torsional relationship at shaft coupling</i> .....	23
Figure 20: <i>dynamic model for test weight determination</i> .....	32
Figure 21: <i>illustration showing geometric similitude of system</i> .....	33
Figure 22: <i>forcing function approximation with shaft z-axis</i> .....	36
Figure 23: <i>spring deflection 5 kg and 10 kg test weights, 25 mm eccentricity</i> .....	37
Figure 24: <i>spring deflection 15 kg and 20 kg test weights, 25 mm eccentricity</i> .....	37
Figure 25: <i>spring deflection 5 kg and 10 kg test weights, 60 mm eccentricity</i> .....	38
Figure 26: <i>spring deflection 15 kg and 20 kg test weights, 60 mm eccentricity</i> .....	38
Figure 27: <i>spring deflection range of frequencies for 15 kg, 25mm eccentricity</i> .....	39
Figure 28: <i>spring deflection range of frequencies for 20 kg, 25mm eccentricity</i> .....	40
Figure 29: <i>spring deflection range of frequencies for 15 kg, 60 mm eccentricity</i> .....	40
Figure 30: <i>spring deflection range of frequencies for 20 kg, 60 mm eccentricity</i> .....	41
Figure 31: <i>graph Sitex® coupling torsional vibration, 10 Nm torque couple</i> .....	45
Figure 32: <i>graph Lovejoy Inc® coupling torsional vibration, 10 Nm torque couple</i> .....	45
Figure 33: <i>illustration of maximum load case on test frame beam</i> .....	46

Figure 34: *properties of test frame section.* .....47  
Figure 35: *maximum load case on motor support beam and section properties.* .....49

## List of Tables

Table 1: <i>parameters for test rig configuration</i> .....	34
Table 2: <i>rotor dimensions and properties for various masses</i> .....	35
Table 3: <i>parameters for Sitex® coupling</i> .....	43
Table 4: <i>parameters for Lovejoy Inc® coupling</i> .....	44
Table 5: <i>table of masses for main frame analysis</i> .....	47
Table 6: <i>table of masses for support frame analysis</i> .....	49

# Notations

## Roman upper case letters

$A$	Rotor
$B$	Bearing housing
$C$	Coupling
$D$	Generator
$E$	Young's modulus; $[\text{kg}\cdot\text{m}^{-1}\cdot\text{s}^{-2}]$
$G$	Shear modulus; $[\text{kg}\cdot\text{m}^{-1}\cdot\text{s}^{-2}]$
$F_{bk}$	Force on bearing from stiffness; $[\text{kg}\cdot\text{m}\cdot\text{s}^{-2}]$
$F_{bc}$	Force on bearing from damping; $[\text{kg}\cdot\text{m}\cdot\text{s}^{-2}]$
$F_l$	Force of inertia load on plane; $[\text{kg}\cdot\text{m}\cdot\text{s}^{-2}]$
$I$	Area moment of inertia; $[\text{kg}\cdot\text{m}^2]$
$I_r$	Area moment of inertia, rotor; $[\text{kg}\cdot\text{m}^2]$
$J$	Polar moment of inertia; $[\text{m}^4]$
$J_r$	Polar moment of inertia, rotor; $[\text{m}^4]$
$J_g$	Polar moment of inertia, generator; $[\text{m}^4]$
$L$	Lagrange equation
$M_g$	Moment about generator shaft; $[\text{kg}\cdot\text{m}^2\cdot\text{s}^{-2}]$
$M_r$	Moment about rotor shaft; $[\text{kg}\cdot\text{m}^2\cdot\text{s}^{-2}]$
$M_{SCK\phi r}$	Moment at shaft coupling, torsional stiffness on rotor; $[\text{kg}\cdot\text{m}^2\cdot\text{s}^{-2}]$
$M_{SCC\phi r}$	Moment at shaft coupling, torsional damping on rotor; $[\text{kg}\cdot\text{m}^2\cdot\text{s}^{-2}]$
$M_{SCK\phi g}$	Moment at shaft coupling, torsional stiffness on generator; $[\text{kg}\cdot\text{m}^2\cdot\text{s}^{-2}]$
$M_{SCC\phi g}$	Moment at shaft coupling, torsional damping on generator; $[\text{kg}\cdot\text{m}^2\cdot\text{s}^{-2}]$
$Q$	Force and moment vector on turbine nacelle
$R$	Raleigh dissipation function
$T$	Kinetic energy or torque; $[\text{kg}\cdot\text{m}^2\cdot\text{s}^{-2}]$
$V$	Potential energy or voltage; $[\text{kg}\cdot\text{m}^2\cdot\text{s}^{-2}$ or $\text{kg}\cdot\text{m}^2\cdot\text{A}^{-1}\cdot\text{s}^{-3}]$

## Roman lower case letters

$c_b$	Linear damping coefficient for bearing housing; $[\text{kg}\cdot\text{s}^{-1}]$
$c_\psi$	Linear damping coefficient for coupling; $[\text{kg}\cdot\text{s}^{-1}]$
$f$	Frequency; $[\text{rad}\cdot\text{s}^{-1}$ or $\text{t}^{-1}]$
$g$	Gravity; $[\text{kg}\cdot\text{m}\cdot\text{s}^{-2}]$

$k_b$	Linear stiffness coefficient for bearing housing; [kg·s <sup>-2</sup> ]
$k_l$	Linear stiffness coefficient; [kg·s <sup>-2</sup> ]
$k_t$	Torsional stiffness coefficient; [kg·m <sup>2</sup> ·s <sup>-2</sup> ·rad <sup>-1</sup> ]
$k_\psi$	Linear stiffness coefficient for coupling; [kg·s <sup>-2</sup> ]
$k_{\phi k}$	Torsional stiffness coefficient for coupling; [kg·m <sup>2</sup> ·s <sup>-2</sup> ·rad <sup>-1</sup> ]
$k_{\phi c}$	Torsional damping coefficient for coupling; [kg·m <sup>2</sup> ·s <sup>-1</sup> ·rad <sup>-1</sup> ]
$l$	Distance from coupling to inertial load or shaft length; [m]
$l_o$	Distance from coupling to rotor centre of gravity; [m]
$l_b$	Distance from coupling to bearing; [m]
$m_r$	Mass of rotor shaft; [kg]
$m$	Mass of inertial load; [kg]
$q_i$	Dimension for dynamic analysis
$q_1$	Rotor shaft angle on plane dimension
$q_2$	Torque angle, rotor shaft dimension
$q_3$	Torque angle, generator shaft dimension
$r$	Radius; [m]
$t$	Time; [s]
$\nu$	Poisson ratio

### Greek letters

$\varepsilon$	Distance to from rotational centre to mass centre; [m]
$\psi$	Rotor shaft angle on plane; [rad]
$\varphi_g$	Torque angle, generator shaft; [rad]
$\varphi_r$	Torque angle, rotor shaft; [rad]
$\omega$	Angular velocity of rotor shaft; [rad·s <sup>-1</sup> ]
$\phi$	Radian angle of twist on shaft; [rad]
$\tau$	Shear stress; [kg·m <sup>-1</sup> ·s <sup>-2</sup> ]
$\mu$	Magnetic permeability; [H·m <sup>-1</sup> ]
$\Omega$	Angular velocity; [rad·s <sup>-1</sup> ]

### Abbreviations

ASME	American Society of Mechanical Engineers
GRC	Gearbox Reliability Collaborative
LSS	Low speed shaft

NREL	National Renewable Energy Laboratory
ODE	Ordinary differential equation
STLE	Society of Tribologists and Lubrication Engineers
SWPTC	Swedish Wind Power Technology Center





# **1 Introduction**

## **1.1 Background**

The global energy industry has seen a marked increase in alternative sources over the past few years. Wind turbines, solar panels, wave and tidal energy schemes are being implemented across Europe and beyond, with intent to create a sustainable energy infrastructure, independent of fossil fuels, and at the same time reduce the carbon footprint of the energy production industry.

The most economical wind energy scheme to date is the land based turbine which can be installed with relative ease almost anywhere a favourable prevailing wind exists. Small to medium sized kW producing turbines and have been in place and generating for decades in such locations as America and Scandinavia. With advances in modern materials and construction techniques, it has become possible to upscale these turbines into multiple MW producers, with equally massive physical dimensions. These large turbines are now seen across Europe and America, both on land and offshore.

Through the application of modern engineering analysis tools and comprehensive recording of operational and failure statistics, it is possible to foresee problems using simulation and statistical techniques. Although these are useful tools for design, they are not necessarily the best option for creating a working physical engineering model. It is imperative that simulation be validated through physical experimentation and qualitative analysis from in-service engineered machines.

A vast repertoire of vibration analysis tools, finite element modelling and failure theory is available to the contemporary engineer and researcher which can be used to specify such important characteristics as forces, stresses, frequencies and vibration modes. These can be applied to the components of a wind turbine, specifically the dynamic parts such as bearings, shafts, gearboxes, brakes, generators and mounting structures.

## **1.2 Objective**

The modern engineering design approach can be broken down into three subsets; the engineering model, mathematical model, and computation model. For this thesis, this approach will be utilised in order to create a physical scaled down model of a wind

turbine drive train, with focus on the vibration and forces created in the bearings, couplings, and gearboxes. The ideal solution will be of a modular and upgradeable design, using simple components and suitable for both intermediate and advanced level experimentation, for both the student and higher level researcher.

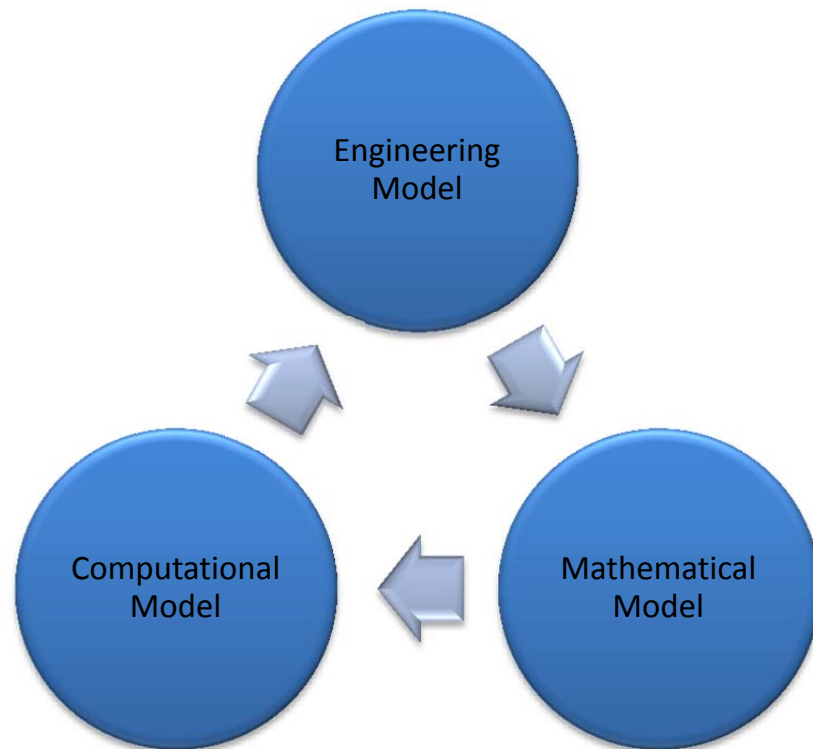


**Figure 1:** *cycle for engineering design.*

### **1.2.1 Engineering Model**

Parameters for the test rig will be determined through analysis of real conditions faced by in-service turbines, modelled on stochastic and varying load excitations, to be used to determine physical scale of components. Determination of parameters will also yield suitable boundaries for the selection of transducers and what signals the test rig will be able to produce.

Development of the model will require the use of an engineering drawing package, such as AutoCad® and other software design tools. The test rig will be located within the Vibrations and Smart Structures Laboratory, at the Division of Dynamics, Chalmers University of Technology, and must comply with local and institutional design and safety standards. Electrical power for the test rig is available through both single and three phase excitation.

### **1.2.2 Mathematical Model**

Upon completion of the engineering model, the constraints of the system will be utilised to create dynamic models which in turn will be used to simulate the response of the system to various excitations and test for any strength or operability limitations which may have arisen during the initial design. Mathematical models will require the parameters of the system for creation of dynamic models starting from first principle. Identification of forces and constraints in free body diagrams will be used with the Lagrange and Newton method to evaluate and develop differential equations of motion.

### **1.2.3 Computational Model**

A thorough examination of the dynamic response, including stress testing, is made possible by a full set of governing system equations. These will be evaluated numerically using Matlab® to determine the operability and limitation of the system. These results will serve as verification to the mathematical models which may present scenarios where the system is not suitable as designed. This final stage of the design may pass or fail the original design, with a failure requiring a return to the engineering model and re-evaluation of the design through the engineering design cycle until satisfactory results are obtained.

## **1.3 Reliability**

Although current and future projects will bring compliance within European and world states to carbon reduction schemes and renewable energy initiatives, governments and utilities face a growing level of public scrutiny over the long term viability and economics of green energy. The underlying concern being the reliability of the power supply and the true life cycle cost of renewable energy; in particular with wind turbines. Former Chief Engineer at the US Governments National Renewable Energy Laboratory (NREL) was quoted as saying the current fleet of wind turbine gearboxes were estimated to be operational for 7-11 years instead of the 20 as designed[1].

Reliability is paramount in wind turbines due to their top heavy composition and the fact that they are often remote and generally inaccessible outwith special consideration as in the case of offshore installations. Maintenance costs are subject to variables such as working environment, location, and equipment requirements for

access; it is not uncommon for the replacement costs of typical mechanical components such as bearings to be up to fifty times that of the component itself [2].

The drive train is the most costly sub assembly in the nacelle, taking up on average 30% [3] of the total cost of installation for a contemporary turbine fleet under 8 MW, inclusive of the generator, gearbox, bearings and shafts. The drive train makes up for 5-15% of the total weight of a typical turbine [4]. Future developments will see the use of much higher rated turbines in the region of 15-20 MW requiring larger and more sophisticated components, including the drive train and gearbox.

## 1.4 NREL Gearbox Reliability Collaborative

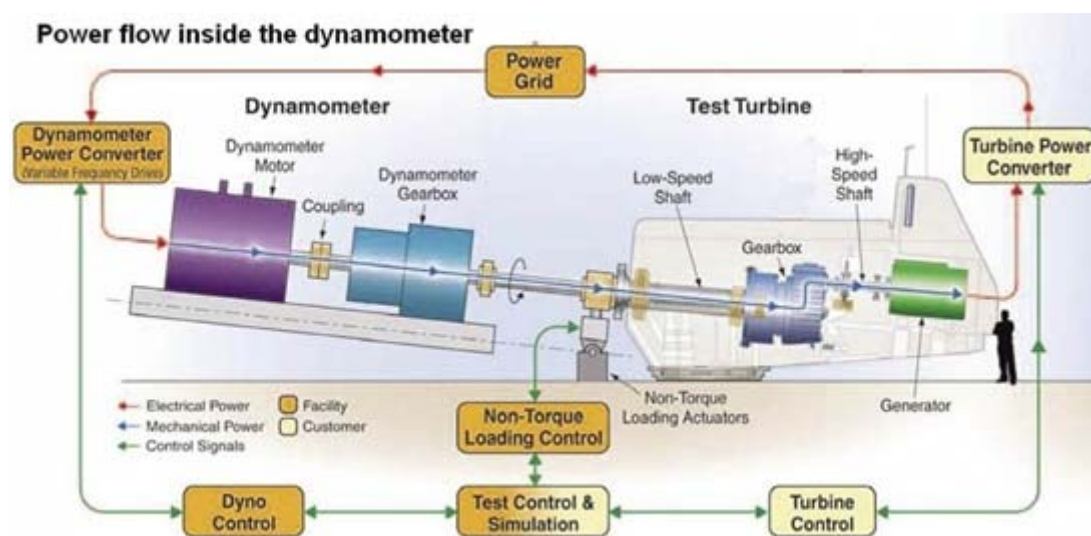


**Figure 2:** NREL dynamometer test bed schematic diagram. [5]

A governmental and industry cross reaching initiative was organised by the US Governments NREL in 2007, referred to as the Gearbox Reliability Collaborative (GRC). A wide range of expertise from academia, industry, and independent researchers was pooled for the purpose of the ongoing study and development into gearbox durability arising from issues associated with the planetary gearboxes in service, due to failures occurring at less than one half of the twenty year design life.

The initial phase of the collaborative study was to focus on the deterioration and failure associated with planet bearings, intermediate shaft locating bearings, and high speed shaft locating bearings, which are considered critical with their failure resulting in a non-functioning gearbox. A three point plan was initiated to study if any design critical loads had not been considered in the original design, to see if any torque and non-torque loadings were acting on the gearbox in an unpredicted manner, and finally

to look at the specifications across the drive train to what, if any, were not selected with the same level of reliability.



**Figure 3:** *NREL dynamometer test facility, Colorado.* [6]

A publicly accessible database of failure modes has been developed by the NREL for both bearings and gears within a planetary gearbox. An ex-service 2.5 MW gearbox which had failed has been taken to their Colorado based facility, repaired and then fitted with a dynamometer and wide array of sensors. This setup allows for various types of loadings to be introduced to the rotor driven LSS of the gearbox, with output data used to verify their analytical models and add to the GRC collective database.

## **1.5 Hansen® Transmission Test Rig**

Hansen Transmissions began construction of a 13.2 MW test rig at their facility in Lommel, Belgium, in 2004, as shown in figure 4. This test bed was designed to better understand the dynamics of its gearboxes in large scale production, which has the gearbox and generation components instrumented allowing for real time analysis of stresses and vibration characteristics.

Design and completion of this large test bed required a multi-stage plan, with the end result being implementation and proving of load cases. The test bed itself is able to simulate various real world loading scenarios for the most common types of indirect

drive, epicyclical gearbox induction generators. There is a facility within the gearing to allow for speed reduction which can be used to simulate the lower speeds and higher torques present in direct drive synchronous generator and hybrid devices currently being rolled out to industry [7].

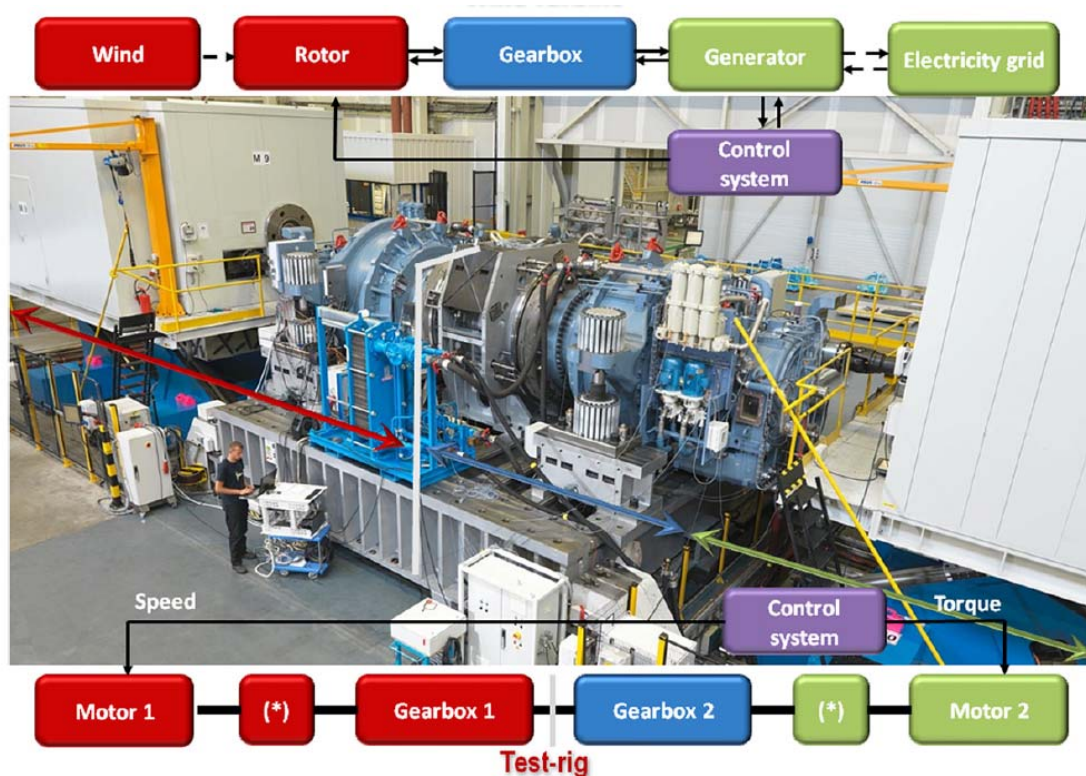


Figure 4: Hansen® 13.2 MW test rig. [8]

## 1.6 Failure Modes

Researchers from industry and the NREL have compiled a database of the most common failure modes in wind turbines. These failures are classified by severity and turnaround time for repairs. This information was made available to the public in an international conference held by the ASME/STLE in 2011. The report highlighted what was considered significant failures by the experts involved, being NREL and Geartech®, through analysis of historical failures. The main findings are that of corrosion on the epicyclical gears, crack propagation through typical failure models, and contact abrasion.

Gears are noted having two common failure modes, which is by fretting corrosion and high cycle bending fatigue located on gear teeth. Fretting corrosion is associated with contacting gear tooth surfaces and small cyclic vibrations between the gears, which is

exacerbated by the fact that while in contact the gear tooth surface receive little to no lubrication. Bending fatigue failure occurs by fast fracture, propagating from areas of stress concentrations on the gear teeth with the direction of inter-granular separation perpendicular to the line of maximum stress. This failure tends to occur at less than yield and at less than  $10^4$  cycles.

Bearings are listed with three common failure modes which are: roller element and raceway hardening cracks, two or three body abrasion, and severe adhesion scuffing. The hardening cracks initiate at the surface and run towards the raceway or element centre. Abrasion is associated with hard particulate contaminants in the lubrication system which in contact with the rollers or raceways and result in smooth, clean gouges and furrows by sliding action of the hardening particles. The adhesion scuffing is a result of materials being repeatedly transferred from roller to raceway by action of friction welding and breaking from surfaces as a result of the large forces associated with the torque multiplication systems associated with gearbox driven wind generation schemes [9].

## **1.7 Motivation for Chalmers Test Rig**

Examination of the common failure modes of wind turbines as detailed in the previous section highlights the negative effects of torsional vibration through the physical manifestation of gear fretting corrosion and scuffing. It is proposed that a suitably strong and scaled down model of the drive train be engineered in order to create similar loadings on components. Sufficient instrumentation is to be installed in order to create useable data whereby simulated models of the system can be validated through real time analysis of the rig.

It is not possible to design on a scale as has been done by NREL, but several key points can be addressed in smaller scale with what is expected to be similar outcomes. Some of the failures are the result of torsional vibration throughout the gearbox and drive train and will be part of the motivation and simulation for the drive train test rig. Other loadings will be introduced, referred to as yaw loads, through externally introduced load irregularities on the drive train from outside forces.

It is envisioned that this test rig will become part of the Vibrations and Smart Structures Laboratory equipment at Chalmers University of Technology, which will be utilised for bachelor and masters level projects and experiments right through to

advanced post doctoral studies. The electrical engineering department has also expressed interested in studying the effects of various loadings on the phase currents within the motor/generator and general studies into basic three-phase induction machine generation.

Chalmers has industrial partnerships with companies working in the wind energy industry such as ABB®, SKF®, various turbine manufacturers, academic intuitions and governmental organisations. The Swedish Wind Power Technology Center (SWPTC) is a Chalmers University of Technology conceived initiative which partners with industry in order create a better understanding of the mechanics of wind turbines. The SWPTC has focus on both mechanical and electrical technology in order develop solutions to better both the efficiency and longevity of the industry, particularly in turbines rated at more than 2 MW, with the focus mainly on the Swedish wind power industry [10].

These partnerships are to be exploited in order to achieve both preferable costing on components and to access information streams which are not immediately accessible in the public domain. It is proposed that his test rig be able to utilise the most modern technology in respect to the generator and motor, instrumentation, data acquisition, software and interpretation. Integration with current industrial condition monitoring equipment will also be considered, as systems such as the SKF® WindCon™ suite are available and used within industry, providing real time analysis of in-service turbines.

Ultimately, the test rig will serve to teach students how to better understand failure mechanisms in order to detect, predict, and prevent failures and faults in a wind turbine drive train. A data base of operation will be established which can be shared within academia and industry, for use in statistical modelling and failure mode analysis methods commonly used in engineering design.

## **1.8 Coordinate System**

In order to correctly assess the forces acting on a wind turbine it is necessary to define the coordinate system for this report. A standard three dimensional orthogonal coordinate system will be used, with the horizontal X axis parallel to the rotor axis, the positive up vertical Z axis parallel to the tower axis, and the right positive Y axis orthogonal to both X and Y axis, as illustrated in the figure 5. Forces on the nacelle

are identified as thrust on the X-axis, weight on the negative Z-axis, and eccentricity on the Y-axis.

For a description of the moments acting on the turbine, it has become standard industry practice to refer to them with the same terminology as aviation industry being yaw about the Z-axis and nacelle pitch about the Y-axis, with the exception of the torque about the X-axis, which would be referred to by an aviator as roll. It is important to note that the term pitch also applies to the blade angle, however, blade pitch angle is not considered in this report.

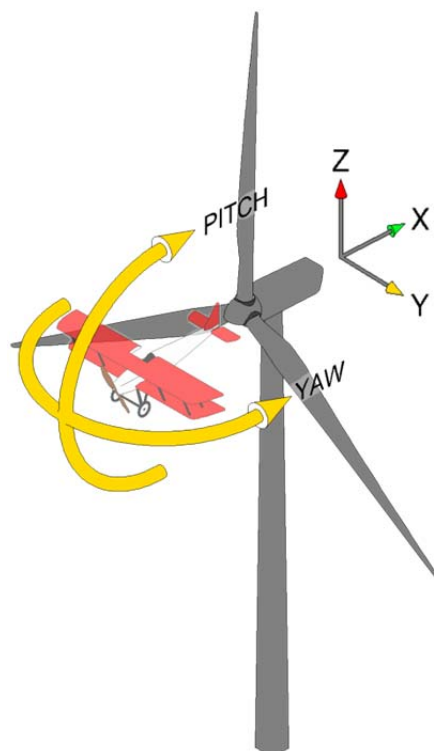


**Figure 5:** *coordinate system for wind turbine.*

The combination of the forces and moments acting on the wind turbine are aligned within a column vector, which is referred to as  $Q$  in equation (1.1) [11].

$$\mathbf{Q} = \begin{Bmatrix} F_x \\ F_y \\ F_z \\ M_x \\ M_y \\ M_z \end{Bmatrix} = \begin{Bmatrix} \text{Thrust} \\ \text{Eccentricity} \\ \text{Weight} \\ \text{Torque} \\ \text{Gyroscopic moment} \\ \text{Yaw moment} \end{Bmatrix} \quad (1.1)$$

## 1.9 Conceptual Design

Chalmers University of Technology has completed some initial design studies in a bachelor level project completed in 2012, with the intent to fabricate a working test rig, with their initial setup shown in figure 6. This setup uses a pair of electric motors, one master and one slave, creating both a driving torque and resisting counter torque. Four bearing housings are shown with two on the rotor shaft and two on the generator shaft. The two shafts are terminated with a pair of spur gears, with the smaller rotor gear pinion driving the larger generator gear.

Adjustment for the system is available by manipulation of the bearing housing springs through positioning and pre-loads, as well as by sliding the bearing housings into position via hold down screws on the test bed. Some preliminary sensor specification was carried out involving inductive type displacement sensors and strain gauges, including their placement and expected results.

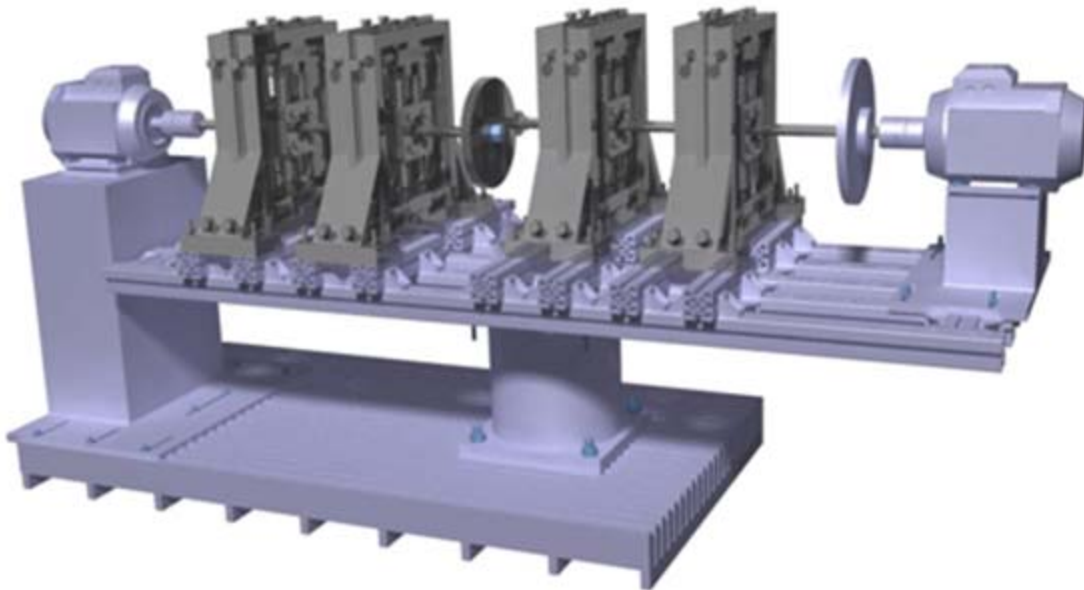


**Figure 6:** *proposed test bed design.* [12]

This design has been expanded upon and the current as built model, developed by the author and staff members of Chalmers University of Technology, is detailed in this report. Engineering drawings, dynamic and stress calculations, sensor selection criteria, data acquisition and prime mover specifications are presented. Select drawings for the project are available in the appendix.

## **1.10 Safety**

The test rig is an electro-mechanical system with many hazards that must be identified. The test rig must be able to operate within design limitations safely with unwanted failure modes designed out. This will be obtained by ensuring stresses, currents and frequencies do not exceed limits by factors of safety, and that personal operating the test rig are at no time subject to hazards as are reasonable practicable. Tools such as risk assessments will be utilised to ensure that personnel are always operating the equipment with safety systems in place, such as barriers, guards, electronic eyes and emergency stop mechanisms.

## **1.11 General Assembly**

Simulation of a wind turbine will be facilitated by the test rig arrangement as shown in Figure 7. This arrangement was developed by the author and Chalmers staff members from the Division of Dynamics, Viktor Berbyuk, Håkan Johansson, and Jan Möller. Considerable design considerations were furthered to create a simple, upgradeable, and modular system.

The test rig consists of a heavy steel test bed, on which the rigid rectangular steel test frame, secured by a bolting arrangement to the test bed. An induction machine and bearing housing are mounted on adjustable sliding support frames which are secured to the test frame with beam clamps.

Adjustment is designed into the test rig, allowing for motion of the motor and bearing in the  $x$  and  $y$ -axis by shifting the motor and housing supports to desired position and securing by tightening the beam clamps. Elevation adjustment of the motor and bearing housing is facilitated by the addition of match drilled shim packing plates, in various thicknesses.

The system shown in figure 7 simulates a typical wind turbine with a direct drive system, with the induction motor taking the place of synchronous generator. Future experiments involving the test rig will utilise an additional motor and bearing housing, which will be mounted in a similar manner as shown, with a more detailed system drawing in the appendix.

The universal coupling is a modular component for the test rig, of which there are three types from different manufacturers. Constraints on the coupling are that it must

be able to compensate for axial misalignment between the rotor shaft and rigid motor coupling, be sufficiently strong to transmit torque as specified by experiment, be electrically isolated from one end to the other, and be easily removable. The coupling shown is a low-torque SITEX® Teeth Coupling model 5/32, consisting of two steel toothed hubs and superpolyamide resin coupling.

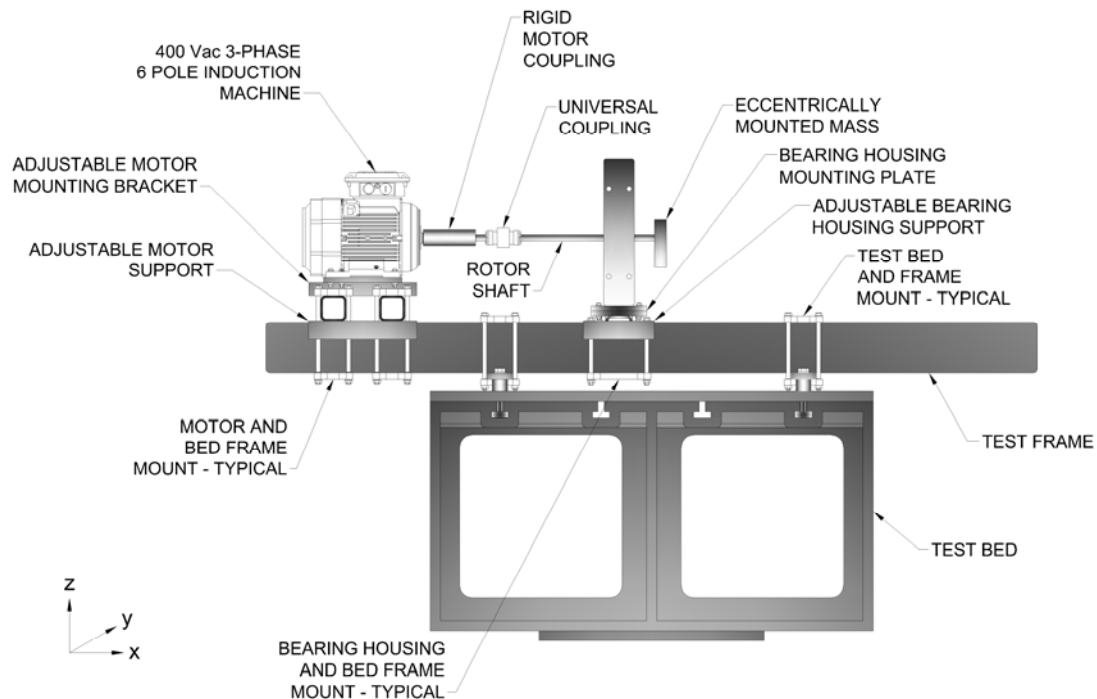


**Figure 7:** complete test rig arrangement, showing one motor and one bearing housing.

The rotor shaft is comprised of Ø25 mm ‘silver steel’ high carbon steel bar, which is both very stiff and very hard, and is typically used in heavy machinery for guide rods, such as with hydraulic rams. The interface between the steel bar and bearing, steel bar and coupling consist of SIT-LOCK® 3 self-centring mechanical compression fittings with Ø25 mm I.D. to Ø35 mm O.D. dimensions, supplied by SITEX®. These provide and axially true, rigid interface between the rotor shaft and bearing or coupling tooth sections. A detailed arrangement drawing of the shaft, shaft coupling, fasteners and hardware is shown in the appendix.

The bearing, which is mounted in the bearing housing assembly, is a double row angular contact bearing, model 3207-BD from Shaeffler®.

## 1.12 3-Phase Induction Motor and Frequency Drive

ABB® is an industrial partner with Chalmers University of Technology and has graciously donated a pair of state of the art motors and controllers for use in the test rig. The qualities that were required for the motor were sufficient power rating for a range of experiments, 3-phase supply for continuous power during operation, and multiple poles for smoother delivery of torque at speed.

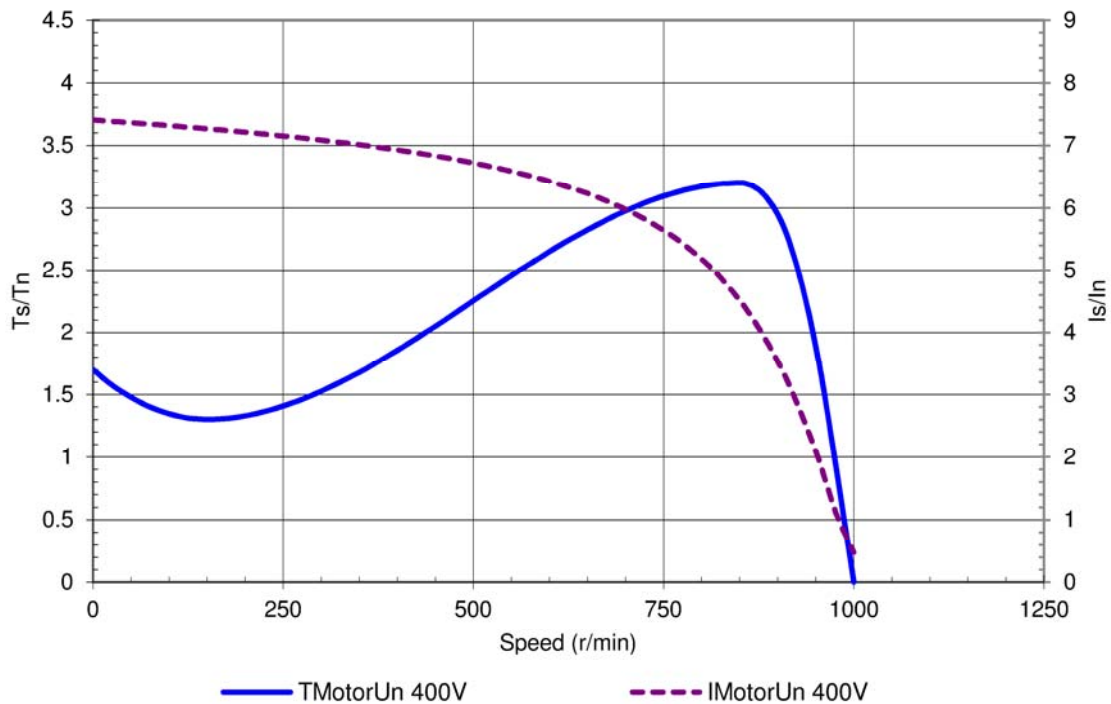


**Figure 8:** *characteristic torque curve for ABB® M3BP-160 motor.*[13]

The motor which was chosen by the author and Chalmers design team was the ABB® M3BP-160-MLA-6. This is a 400 V AC, 3-phase, 6-pole induction machine, with integral shaft encoder, energised from an ABB® ACS-550-01-015A-4 V/f frequency drive unit, with speed, position, and torque control. Characteristic torque and current for the motor is shown in figure 8, which is typical for a deep bar/double cage, squirrel cage induction machine. The torque is shown as a ratio of starting torque to nominal torque, dropping to zero at synchronous speed, in this case, 1000 rpm at 400 V AC.

As discussed, two motors and controllers have been issued to Chalmers® to facilitate both the initial, one motor test setup, and future iterations which will require coupled torque pairs via coupled motors. Each motor is fitted with a heavy duty, IP rated Leine & Linde® pulse tachometer, consisting of a 2048 tick resolution incremental encoder,

capable of detecting position to  $3.067 \times 10^{-3}$  rad [0.176°], which can operate up to 6000 rpm. This will interface with a tacho-pulse module in the ACS550 frequency drive, also supplied by ABB®.

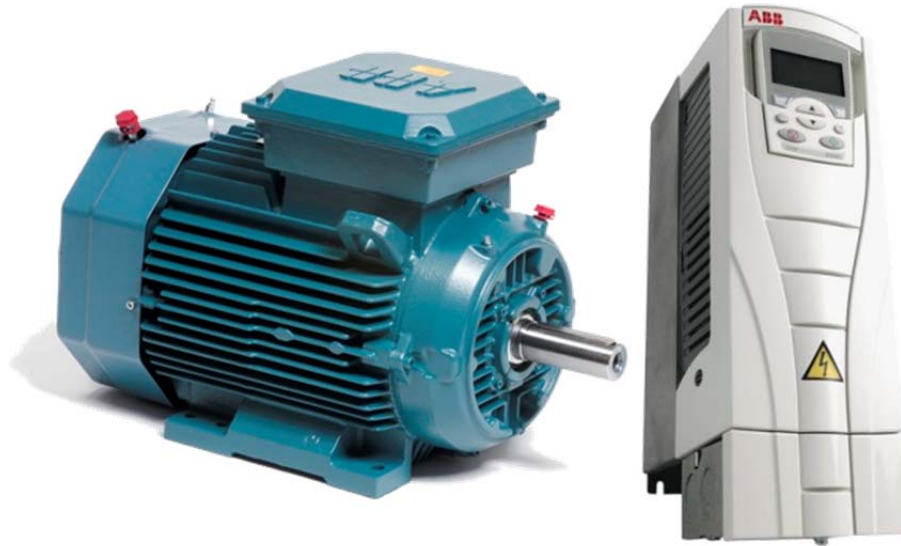


**Figure 9:** ABB® motor and variable frequency drive controller. [14][15]

The ACS550 frequency drive unit is capable of 7.5 kW power delivery, using vector control with integral brake chopper and swinging choke circuitry. The control interface consists of a front panel pushbutton system or remote through standard Ethernet protocol and proprietary ABB® software.

## Further Details on Components

Only a brief overview of the components has been given in this report. More details in regards to specifications, materials, dimensions, and power requirements can be found in the product specific literature. Further details on all components are available by contacting the Division of Dynamics at Chalmers University of Technology, and by visiting the respective manufacturer's corporate websites.

### 1.13 System Block Diagram

An overview of the complete working system for setup 1 is shown in Figure 10. Overall control and data acquisition is facilitated by a personal computer with National Instruments® Labview® software installed. This is connected to a National Instruments® cDAQ-9178 eight position data bus module, utilising standard Universal Serial Bus (USB) protocol for communications.

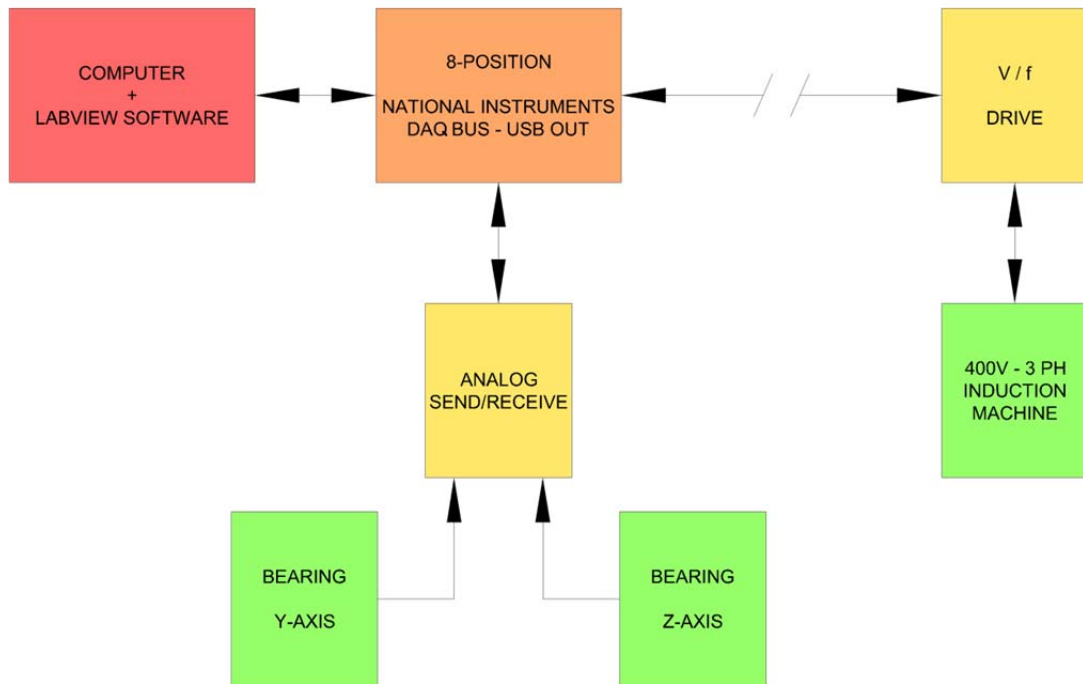


**Figure 10:** system block diagram for wind turbine test bed, measuring Y and Z axis.

The y and z axis linear displacement sensors are powered by a bus mounted National Instruments® NI-9207 module, 16 channel (8 voltage + 8 current),  $\pm 10$  VDC,  $\pm 20$  mA analogue module supplying DC output to the sensors, which also receives the AC position signal dependent input data. This module will allow all signals from the first experimental setup to be acquired, leaving 7 slots available for future upgrades and alterations to the existing design.



**Figure 11:** National Instruments® cDAQ-9178 [16]

All data will be recorded on the computer, preferably in Microsoft® Excel™ formatting, to be analysed by further software packages such as Mathworks®

Matlab®. The eight position National Instruments® bus allows for further signal acquisition in future iterations of the test rig set up and subsequent experiments.

### 1.13.1 Displacement Sensor Arrangement

In order to determine the dynamic response of the bearing housing it is necessary to install some transducers. For the initial testing phase of the test rig two linear non-contact displacement sensors are mounted to the bearing housing which will be used to determine the forces acting on the bearing. Aluminium brackets are installed onto the face of the bearing housing, aligned with the centre of the bearing on the y and z axis. Aluminium was chosen on the mounting brackets to reduce signal attenuation by minimising flux absorption by aluminium's lower characteristic magnetic permeability ( $\mu$ ).

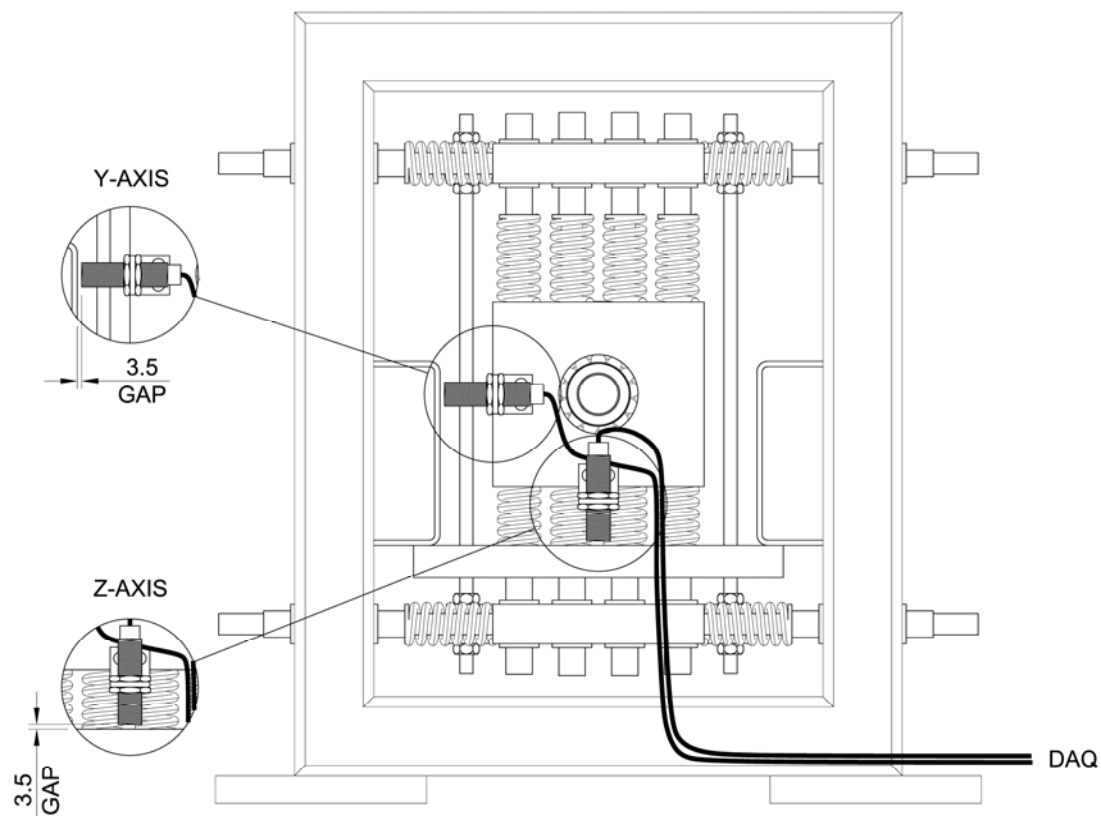


**Figure 12:** arrangement of the displacement sensors and cabling, with data flow to data acquisition module.

Omega® model LD701-2/5 three wire linear displacement sensors have a range of 2 to 5 mm, with a repeatability of  $\pm 10 \mu\text{m}$  and switching frequency of 1000 Hz. They are driven by a 14-30 V DC supply with an analogue output on the third wire sent to

the National Instruments® data acquisition module, which will be input to Labview® software for analysis and recording.

## 1.14 Bearing Housing

### 1.14.1 Physical Arrangement

Chalmers University has designed a dynamic bearing housing, which consists of a steel frame, steel helical springs and centrally mounted roller bearing, as shown in Figure 13. This has been modified by the author to allow for fitting of displacement sensors.

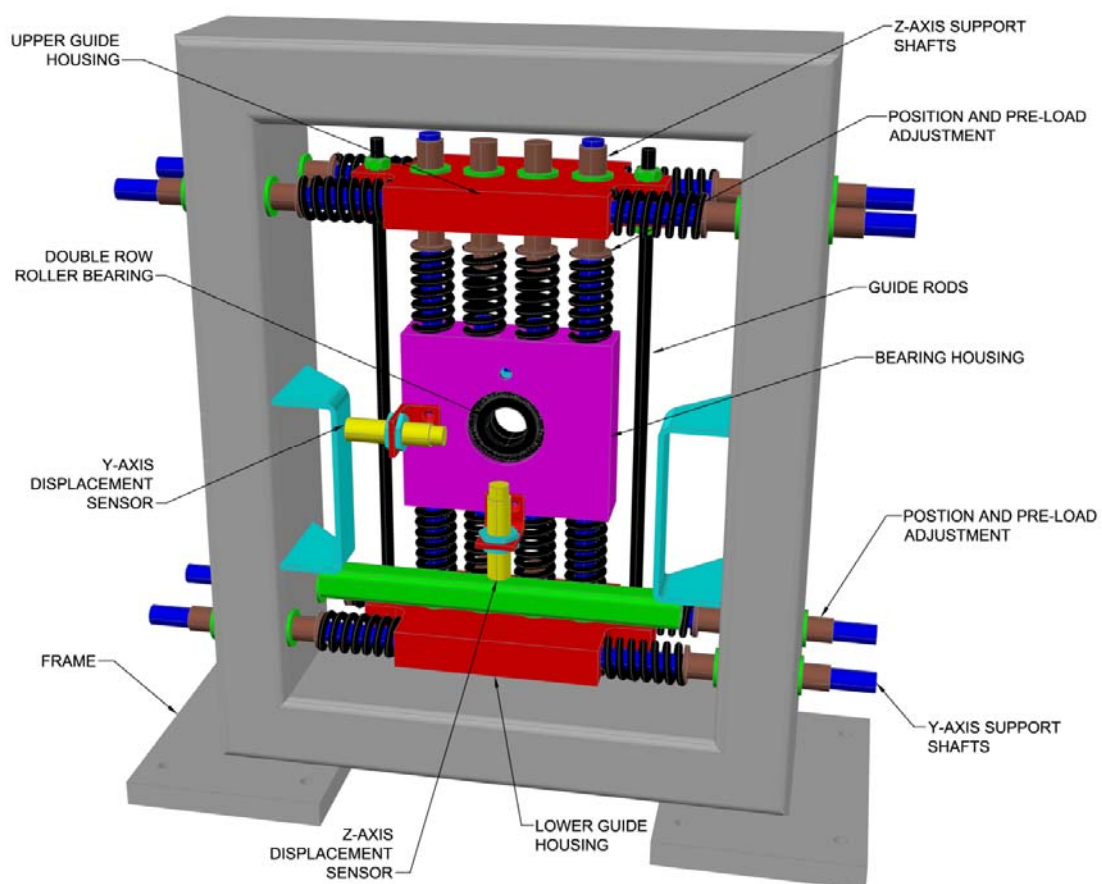


**Figure 13:** *arrangement of the bearing housing with displacement sensors installed, shown from the front face.*

Both horizontal and vertical motion of the bearing is facilitated along free running high tensile steel support shafts which are mounted with helical springs, captivated between the upper and steel lower guide housings and frame. Two high tensile steel guide rods are rigidly mounted between the upper and lower guide housing to provide

support for the system during assembly. The upper and lower guide housings have through holes to allow free running of the  $y$  axis support shafts.

The aluminium centre bearing housing section has a through hole and counter bore which allows for a standard roller bearing to be mounted. Two vertically mounted holes on each side allow the  $z$  axis support shafts to pass freely. The bearing is held in place with a covering plate and four screws, which is not shown due to the frame orientation in Figure 13. Full schematics for the bearing housing are available from the Division of Dynamics at Chalmers University of Technology.

### 1.14.2 Bearing Housing Equivalent Mechanical Model

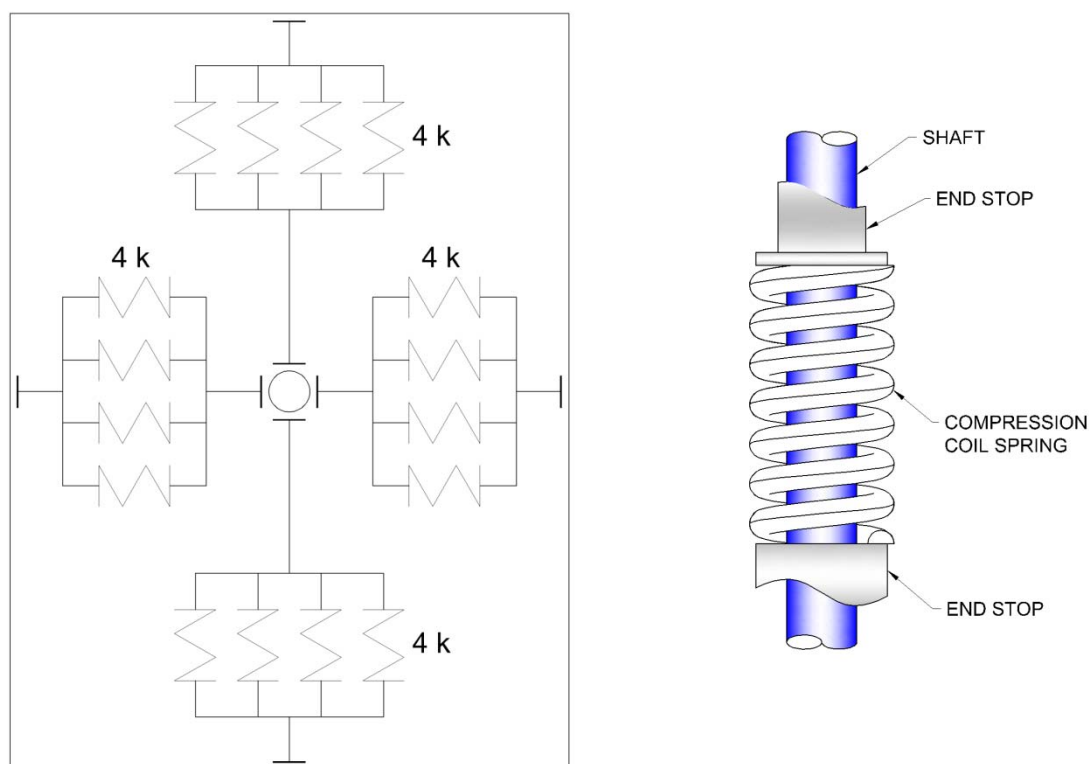


**Figure 14:** *equivalent model of bearing housing and spring retention system.*

The support shafts are fabricated high tensile steel with threaded ends, on which nuts and threaded bushings are mounted to allow for position adjustment, as well as spring pre-load adjustment. These are mounted into the frame through clearance holes, and adjusted by means of nut placement on the bushings.

The frame is fabricated from rectangular hollow section (RHS) and joined at the corners with  $45^\circ$  mitre joints, with the corners are welded all round. The frame is mounted into the test rig through the two integral mounting pads, which are welded all

round to the lower face of the frame. These two mounting pads allow the frame to be secured to the test rig using standard M12 nuts and bolts, four per pad.

The equivalent model of the bearing housing frame is shown in figure 14. There are pairs of four parallel compression coil springs across both the  $y$  and  $z$  axis, with two different loading criteria, whereby the stiffness can be calculated.

The first case is when the springs are not pre-loaded; these springs are strictly held in place by compression and will not affect the system should the static spring length be exceeded through normal operation. The second case is with pre-loading in the springs.

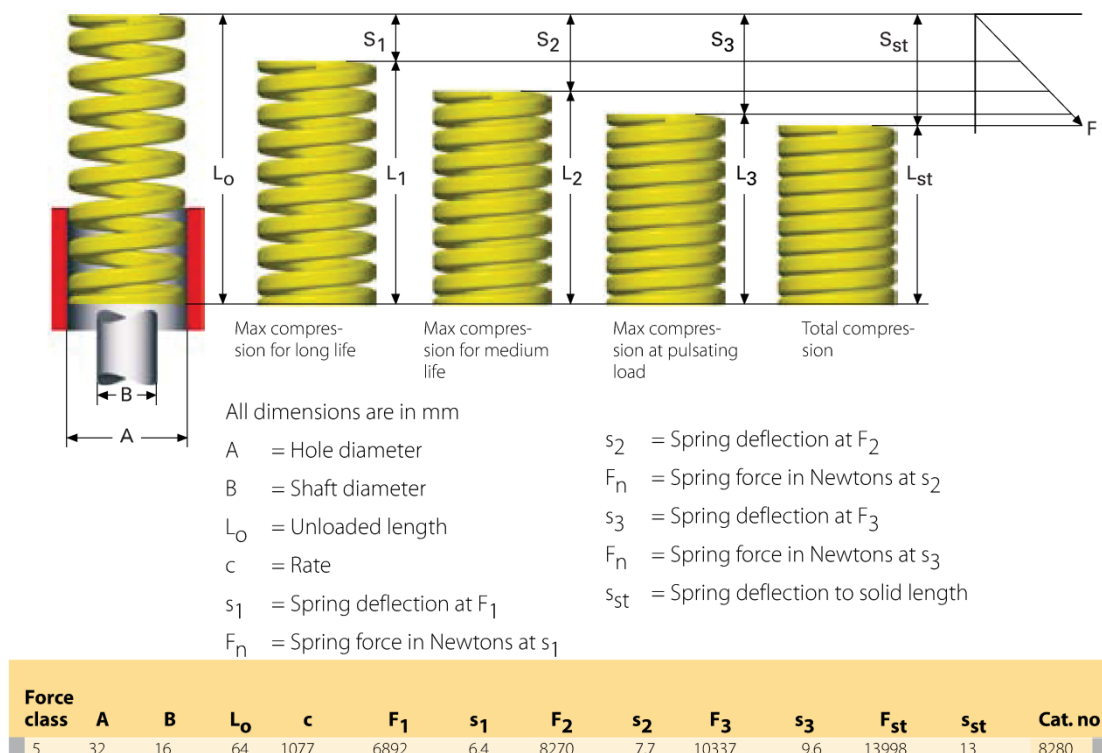


**Figure 15:** Lesjöfors™ spring specification, with stiffness coefficient 'c' in N/mm, forces ' $F_n$ ' in N, and dimension ' $s_n$ ' in mm. [17]

The two cases can be numerically solved by examination of the bearing housing arrangement and application of Hooke's Law. In the non-pre loaded case, the stiffness across each axis will equal  $4k$ , and in the pre-loaded case the stiffness will be  $8k$ , with both solutions only valid in static equilibrium. The manufacturer's specification for the spring coefficient is  $1077 \text{ kN/m}$  per spring. Using the above simplification and the manufacturers rating the stiffness coefficients for the  $y$  and  $z$  axis for the first, non-

preload case is 4308 kN/m, and 8616 kN/m (plus compression stiffness variations over displacement  $4kx$ ) for the pre-loaded case.

Although the stiffness can be calculated in static equilibrium, the true dynamic stiffness of the spring will vary according to the curve as specified by manufacturer, as shown in figure 15, with stiffness typically increasing in a non-linear fashion as the springs are compressed. The spring curve will therefore introduce a non-linear stiffness which can be estimated by the manufacturer's specification, but need to be determined experimentally. There exists a third case, where a pre-loaded spring setup sees the one set of springs meet their natural length during operation, where the stiffness will change between  $4k$  and  $8k$  depending on position. This is a non-linear case and will not be studied in this report.

### 1.15 Test Rig Quasi-Static Model – Setup 1

Figure 16 shows the arrangement for the test rig model, in quasi-static condition with input shown on the left side via the rotor (A), passing through the bearing housing (B), universal shaft coupling (C), and to the generator (D).

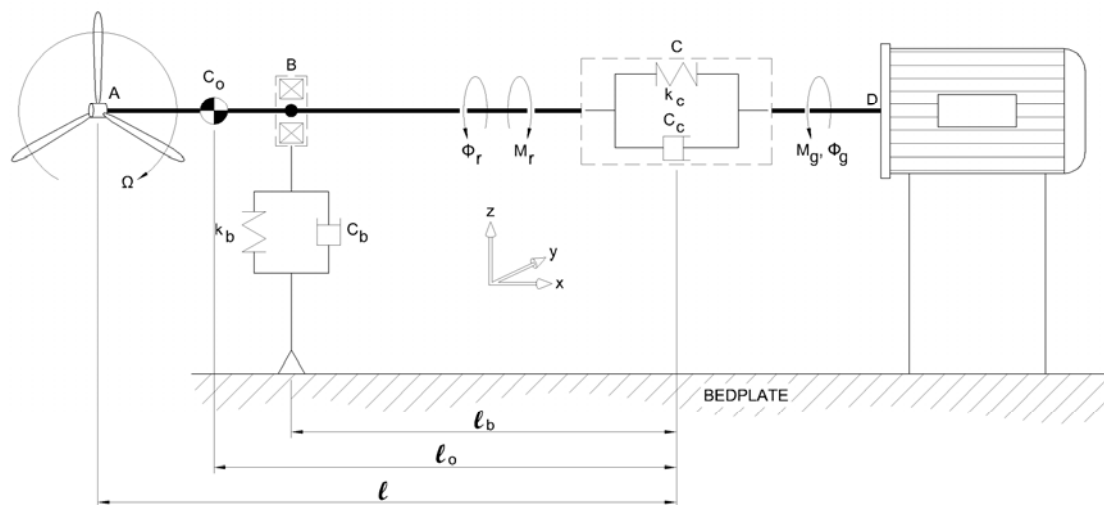


*Figure 16: illustration showing the static model of the test rig, complete with rotor, shafts, bearing, coupling, and generator, setup 1.*

The Chalmers drive train test rig will initially use the motor as input with an out of balance mass installed on the rotor end of the shaft; this will not affect the overall dynamics of the system. Both the coupling and the bearing housing have stiffness and damping coefficients which will be determined through analytical and experimental means. The motor have some stiffness and damping, but for the initial testing and

setup of the test rig, it will be assumed the motor and mounting system is perfectly rigid. This model is assumed to have rigid shafts, with only a torque input at the rotor and only a load moment at the generator. The rotor shaft (A through C) has a mass and inertia.

The coupling will be analogous to the unity gearing and coupling present in a direct drive (synchronous) type wind turbine. It will introduce a torsional misalignment to be determined in Setup 1.

### 1.16 Test Rig Dynamic Model – Setup 1

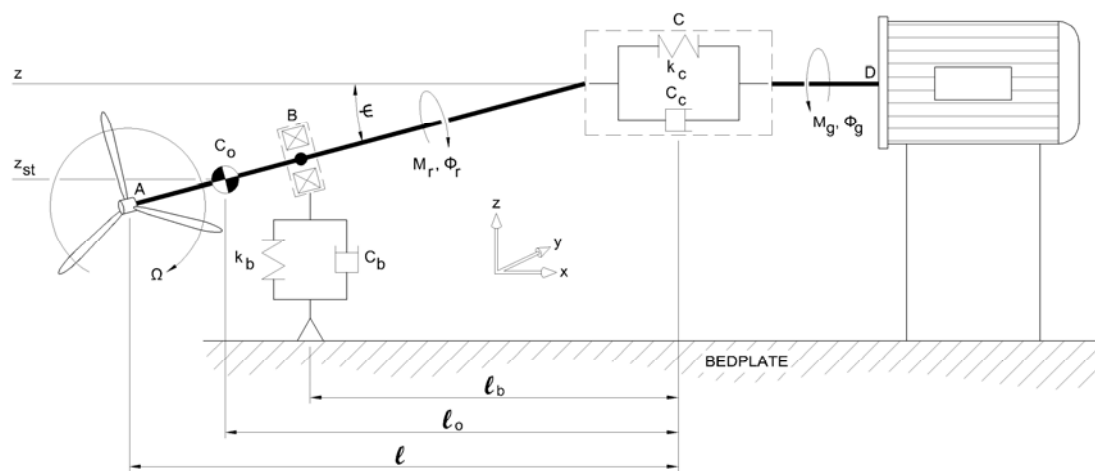


**Figure 17:** *dynamic model of test rig with rotor shaft angle, setup 1.*

Initial testing of the test rig will focus on the relationship between the rotor shaft angle in relation to the quasi-static and unloaded normal axis. A periodic sinusoidal load is introduced at the rotor which will act to displace the bearing, with the arrangement shown in figure 17. Only motion on the  $z$  axis will be analysed, and all angles are assumed to be small, ie,  $\sin(\theta) \approx \theta$ .

The displacement sensors located on the bearing housing, as shown in figure 12 will track the motion of the bearing in the  $z$  axis, and by using the geometry of the system it will be possible to physically measure the angle.

In lieu of actually setting up a functional rotor blade unit, an inertia load in the form of an eccentrically mounted mass is mounted to point (A). The mass for the test load will be determined numerically once the equations of motion and variables are fully defined, and methodology is detailed in section 3 of this report.

## 1.17 Rotor Out of Balance Forcing Function Dynamic Model

Figure 18 shows the arrangement of the rotor and bearing housing in the  $y$  and  $z$  plane. A periodic sinusoidal force will be developed for the  $z$  axis to simulate the various forces created by the rotor, as function of the mass  $m$ , rotational speed of the rotor  $\Omega$ , and the rotor out of balance centroid distance the neutral axis  $\epsilon$ .

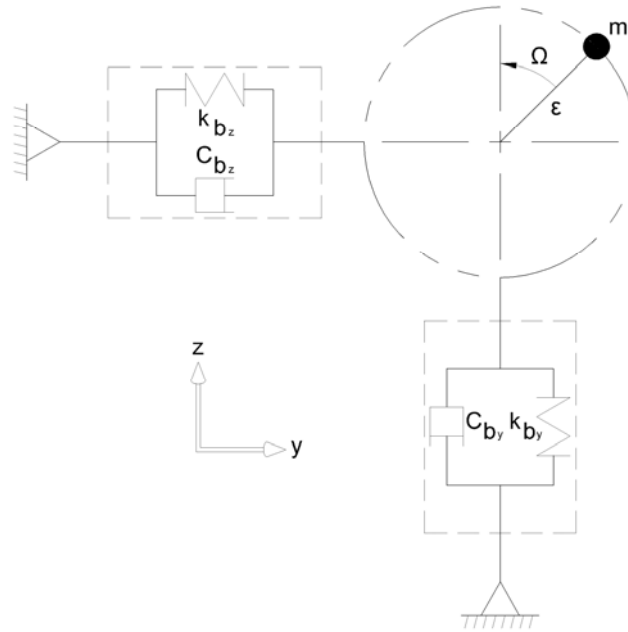


**Figure 18:** *eccentric mass setup for test rig inertia load case.*

The bearing frame has both  $y$  and  $z$  axis mounted springs, however, for test setup 1 analysis only the vertical  $z$  axis motion will be utilised. Although no dampers have been installed in the bearing frame, the system itself will have some degree of damping, which will be determined experimentally as mentioned previously.

## 1.18 Coupling Dynamic Model

Figure 19 shows the arrangement of the coupling. Several coupling types are going to be used in the test rig, all with different qualities. There are some pre-requisites for the choice of coupling to consider more than just the ability to handle torque and speed. The test rig will see strain gauges affixed to the rotor shaft for future works, so electrical isolation is a requirement to prevent flux from the electric motor contaminating the gauge.

Two couplings were sourced for the initial testing of the rig, one from SITEX® and one other from Lovejoy™. Both have a non-conductive flexible element between

rigid connections to the shafts. Determination of the properties of the flexible element, such as torsional stiffness and damping, will be made through examination of the geometry and material properties. This data will be used to create simulations from the mathematical models and will be confirmed from examination and comparison with experimental data, shown in detail in section 3.2.

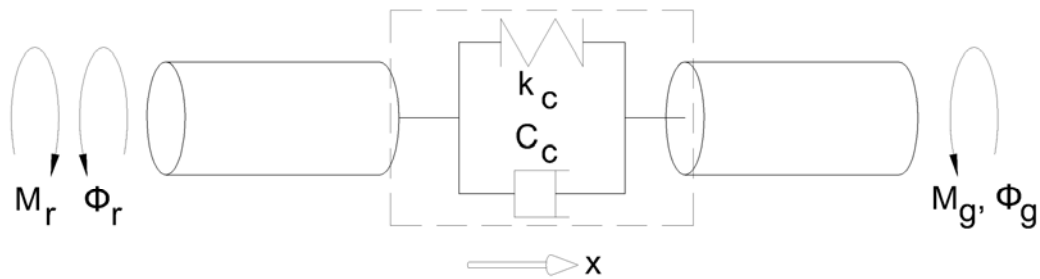


**Figure 19:** *torsional relationship at shaft coupling.*

The coupling serves as an analogue to the unity gearing arrangement typically found in synchronous, direct drive wind turbines. In future iteration of the test rig, this can be replaced with any suitable coupling, and even a gearbox. Most turbines use an inline, shaft mounted, disc brake arrangement between the coupling/gearbox and generator, so this is also an optional upgrade to the test rig. Experiments involving the measuring of torque angles can be facilitated by affixing strain gauges to the coupling and shaft using traditional instrumentation techniques.

## 2 Test System 1 Differential Equations of Motion

A governing system of differential equations is required to analyse the performance and motion of the test rig for test setup 1. These are developed making the assumptions of rigid rotor and generator shafts, small angles, and set up using three distinct and measurable dimensions, as detailed in the following set of equations. Setup 2 of the test rig involves a second, identical set of motors and shafts, mounted at  $180^\circ$  to the first setup on the other end of the frame, to be used for parallel spur gear pair experiments. These equations are applicable to both arrangements..

### 2.1 System Formulas

Variables for the system are selected from the dynamic model shown in figure 17. The neutral axis in line with the generator axis, denoted as  $\mathbf{z}$  on the drawing. A static deflection exists due to self mass on the rotor shaft and bearing housing spring, creating a static offset,  $\mathbf{z}$  static.

Defining the dimensions: rotor shaft angle  $\psi$ , rotor shaft torque angle  $\varphi_r$ , generator torque shaft angle  $\varphi_g$ ;

$$\mathbf{q} = \begin{Bmatrix} \psi \\ \varphi_r \\ \varphi_g \end{Bmatrix} = \begin{Bmatrix} q_1 \\ q_2 \\ q_3 \end{Bmatrix} \quad (1.2)$$

By assuming small angle  $\psi$ , we also have small values for  $\mathbf{z}$ ;

$$\frac{z}{l_o} = \tan(\psi) \approx \psi \quad (1.3)$$

$$\frac{\dot{z}}{l_o} \approx \dot{\psi} \quad (1.4)$$

$$\frac{\ddot{z}}{l_o} \approx \ddot{\psi} \quad (1.5)$$

Kinetic energy of the system;

$$T = \frac{1}{2} I_r \dot{\psi}^2 + \frac{1}{2} m_r (l_o \dot{\psi})^2 + \frac{1}{2} J_r \dot{\varphi}_r^2 + \frac{1}{2} J_g \dot{\varphi}_g^2 \quad (1.6)$$

Potential energy of system;

$$V = \frac{1}{2}k_\varphi(\varphi_g - \varphi_r)^2 + \frac{1}{2}k_\psi\psi^2 + \frac{1}{2}k_b\varphi_r^2 + \frac{1}{2}k_b(l_b\psi - z_{st})^2 + m_r g l_o \psi \quad (1.7)$$

Dissipation function for system;

$$R = \frac{1}{2}C_\varphi(\dot{\varphi}_g - \dot{\varphi}_r)^2 + \frac{1}{2}C_\psi\dot{\psi}^2 + \frac{1}{2}C_b\dot{\varphi}_r^2 + \frac{1}{2}C_b(l_b\dot{\psi})^2 \quad (1.8)$$

Non-conservative forces, with linear force referenced at centre of gravity;

$$Q_{1(z)} = F(t, \psi)l \Big|_{x=l_w} = \frac{l}{l_o} F(t, \psi, z) \Big|_{x=l_o} \quad (1.9)$$

$$Q_{2(r)} = -M_r(t, \varphi_r) \quad (1.10)$$

$$Q_{3(g)} = M_g(t, \varphi_g) \quad (1.11)$$

Development of the Lagrange equation,  $L = T - V$ ;

$$L = \frac{1}{2}(I_r\dot{\psi}^2 + m_r(l_o\dot{\psi})^2 + J_r\dot{\varphi}_r^2 + J_g\dot{\varphi}_g^2) - \frac{1}{2}(k_\varphi(\varphi_g - \varphi_r)^2 + k_\psi\psi^2 + k_b\varphi_r^2 + k_b(l_b\psi)^2) + m_r l_o g \psi \quad (1.12)$$

Partial differential equations of system, understanding that sum of work done through spring static deflection and system cancel using Newton's second law, i.e.  $k_b z_{st} = m_r g l_o$ ;

$$\frac{\partial L}{\partial \dot{\psi}} = I_r \dot{\psi} + m_r l_o^2 \dot{\psi} + J_r \dot{\varphi}_r + J_g \dot{\varphi}_g \quad (1.13)$$

$$\frac{d}{dt} \left( \frac{\partial L}{\partial \dot{\psi}} \right) = I_r \ddot{\psi} + m_r l_o^2 \ddot{\psi} + J_r \ddot{\varphi}_r + J_g \ddot{\varphi}_g \quad (1.14)$$

$$\frac{\partial L}{\partial \psi} = -(k_\varphi(\varphi_g - \varphi_r) + k_\psi\psi + k_b\varphi_r + k_b l_b^2 \psi) \quad (1.15)$$

$$\frac{\partial D}{\partial \psi} = C_\varphi(\dot{\phi}_g - \dot{\phi}_r) + C_\psi \dot{\psi} + C_b \dot{\phi}_r + C_b l_b^2 \dot{\psi} \quad (1.16)$$

Development of the final equations,  $\frac{d}{dt} \left( \frac{\partial L}{\partial \dot{q}_i} \right) + \frac{\partial R}{\partial \dot{q}_i} - \frac{\partial L}{\partial q_i} = Q_i$ , for the three coordinates;

$$(I_r + m_r l_o^2) \ddot{\psi} + (C_\psi + C_b l_b^2) \dot{\psi} + (k_\psi + k_b l_b^2) \psi = F(t, \psi, z) l \quad (1.17)$$

$$J_r \ddot{\phi}_r + C_\varphi(\dot{\phi}_r - \dot{\phi}_g) + C_b \dot{\phi}_r + k_\varphi(\phi_r - \phi_g) + k_b \phi_r = -M_r(t, \phi_r) \quad (1.18)$$

$$J_g \ddot{\phi}_g + C_\varphi(\dot{\phi}_g - \dot{\phi}_r) + k_\varphi(\phi_g - \phi_r) = M_g(t, \phi_g) \quad (1.19)$$

Rewriting equation (1.17) in terms of  $\mathbf{z}$ ;

$$(I_r + m_r l_o^2) \ddot{z} + (C_\psi + C_b l_b^2) \dot{z} + (k_\psi + k_b l_b^2) z = F(t, \psi, z) l \cdot l_o \quad (1.20)$$

Equations (1.18), (1.19), and (1.20) now fully define the system for setup 1. In order to analyse and simulate the system, parameters must be assigned to all variables.

## 2.2 Dynamic Analysis

Some variables are available through direct measurement, are supplied by manufacturer, or, otherwise determined through simulation or experiment. The complete set of forces and moments acting on the system is detailed as follows:

$$F_{bk}(t) = k_b l_b^2 l_o z \quad ; \text{ force on bearing from spring} \quad (1.21)$$

$$F_{bc}(t) = C_b l_b^2 l_o \dot{z} \quad ; \text{ force on bearing from damping} \quad (1.22)$$

$$F_l(t) = m \varepsilon \omega^2 l \quad ; \text{ force of inertia load on plane} \quad (1.23)$$

$$M_{bk\varphi r}(t) = k_b \phi_r \quad ; \text{ moment at bearing from torsional stiffness} \quad (1.24)$$

$$M_{bc\varphi r}(t) = c_b \dot{\phi}_r \quad ; \text{ moment at bearing from} \quad (1.25)$$

torsional damping

$$M_{SCk\varphi r}(t) = k_\varphi(\varphi_r - \varphi_g) \quad ; \text{ moment at shaft coupling from torsional stiffness on rotor} \quad (1.26)$$

$$M_{SCc\varphi r}(t) = C_\varphi(\dot{\varphi}_r - \dot{\varphi}_g) \quad ; \text{ moment at shaft coupling from torsional damping on rotor} \quad (1.27)$$

$$M_{SCk\varphi g}(t) = k_\varphi(\varphi_g - \varphi_r) \quad ; \text{ moment at shaft coupling from torsional stiffness on generator} \quad (1.28)$$

$$M_{SCc\varphi g}(t) = C_\varphi(\dot{\varphi}_g - \dot{\varphi}_r) \quad ; \text{ moment at shaft coupling from torsional damping on generator} \quad (1.29)$$

N.B. For the initial parameterisation of the system the damping forces will not be considered for ease of calculation, and, to present the worst case operating scenario in terms of acceleration and displacements.

### 2.3 Initial Conditions

All calculations will assume the system to initially be in static equilibrium, therefore the displacement and angle of the shaft will be zero.

$$\psi \Big|_{t=0} = 0 \rightarrow z l_o \Big|_{t=0} = 0$$

$$\dot{\psi} \Big|_{t=0} = 0 \rightarrow \dot{z} l_o \Big|_{t=0} = 0$$

### 2.4 Semi-Inverse Dynamic Analysis

Often one or more of the variables is unknown; however, in the case with coupled equations it is possible to solve the system through algebraic manipulation if some of the key variables are known. For study of test setup 1, the torque angles of generator and rotor are coupled, and system equations (1.18) and (1.19) can be stated as follows:

$$J_r \ddot{\varphi}_r = C_\varphi \Delta \dot{\varphi} - C_b \dot{\varphi}_r + k_\varphi \Delta \varphi - k_b \varphi_r - M_r(t) \quad (1.30)$$

$$J_g \ddot{\varphi}_g = -C_\varphi \Delta \dot{\varphi} - k_\varphi \Delta \varphi + M_g(t) \quad (1.31)$$

With the torsional misalignment expressed as;

$$\Delta\varphi = \varphi_g(t) - \varphi_r(t) \quad (1.32)$$

Equation for the rotor torque angle (1.30) can be re-written as;

$$J_r\ddot{\varphi}_g - J_r\ddot{\varphi}_r = -C_\varphi\Delta\dot{\varphi} + C_b\dot{\varphi}_r - k_\varphi\Delta\varphi + k_b\varphi_r + M_r(t) + J_r\ddot{\varphi}_g \quad (1.33)$$

Discounting the effect of bearing damping and stiffness;

$$J_r\Delta\ddot{\varphi} + C_\varphi\Delta\dot{\varphi} + k_\varphi\Delta\varphi = M_r(t) + J_r\ddot{\varphi}_g \quad (1.34)$$

Case A – Generator torque angle and rotor moment known;

$$\varphi_g(t) = \varphi_g^o(t)$$

$$M_r(t) = M_r^o(t)$$

Equation (1.34) can be expressed as;

$$J_r\Delta\ddot{\varphi} + C_\varphi\Delta\dot{\varphi} + k_\varphi\Delta\varphi = M_r^o(t) + J_r\ddot{\varphi}_g^o(t) \quad (1.35)$$

With a known  $\Delta(t)$  and equation (1.32),  $\varphi_r(t)$  can be determined as can  $M_g(t)$  from equation (1.31). In the case of a constant angular velocity for the rotor, which is often the applicable to a wind turbine system, the torque goes to zero in the second derivative,  $J_r\ddot{\varphi}_g(t) = 0$ , further simplifying the solution;

$$J_r\Delta\ddot{\varphi} + C_\varphi\Delta\dot{\varphi} + k_\varphi\Delta\varphi = M_r^o(t) \quad (1.36)$$

Equation for the generator torque angle (1.31) can be re-written as;

$$J_g\ddot{\varphi}_g - J_g\ddot{\varphi}_r = -C_\varphi\Delta\dot{\varphi} - k_\varphi\Delta\varphi + M_g(t) - J_g\ddot{\varphi}_r \quad (1.37)$$

$$J_g\Delta\ddot{\varphi} + C_\varphi\Delta\dot{\varphi} + k_\varphi\Delta\varphi = M_g(t) - J_g\ddot{\varphi}_r \quad (1.38)$$

Case B – Rotor torque angle and generator moment known;

$$\varphi_r(t) = \varphi_r^o(t)$$

$$M_g(t) = M_g^o(t)$$

Equation (1.38) can be expressed as;

$$J_g \Delta \ddot{\varphi} + C_\varphi \Delta \dot{\varphi} + k_\varphi \Delta \varphi = M_g^o(t) - J_g \ddot{\varphi}_r^o(t) \quad (1.39)$$

As in the previous case, a known  $\Delta(t)$  and equation (1.32),  $\varphi_g(t)$  can be determined as can  $M_r(t)$  from equation (1.34). Also, as with the previous case, the torque goes to zero in the second derivative,  $J_g \ddot{\varphi}_r = 0$ , for a simpler solution;

$$J_g \Delta \ddot{\varphi} + C_\varphi \Delta \dot{\varphi} + k_\varphi \Delta \varphi = M_g^o(t) \quad (1.40)$$

Case C – Direct dynamics problem;

$$M_g(t) = M_g^o(t)$$

$$M_r(t) = M_r^o(t)$$

$$\varphi_g(0) = \varphi_g^o; \quad \dot{\varphi}_g(0) = \dot{\varphi}_g^o$$

$$\varphi_r(0) = \varphi_r^o; \quad \dot{\varphi}_r(0) = \dot{\varphi}_r^o$$

Given these moments and initial conditions, it is possible to solve for  $\varphi_g(t)$ ,  $\varphi_r(t)$ , and  $\Delta(t)$ , discounting the effect of any bearing damping or stiffness;

$$J_r \ddot{\varphi}_r = C_\varphi (\dot{\varphi}_g - \dot{\varphi}_r) + k_\varphi (\varphi_g - \varphi_r) - M_r^o(t) \quad (1.41)$$

$$J_g \ddot{\varphi}_g = -C_\varphi (\dot{\varphi}_g - \dot{\varphi}_r) - k_\varphi (\varphi_g - \varphi_r) + M_g^o(t) \quad (1.42)$$

This system of ODE's can be used to determine outstanding variables and parameters in the system. If the effects of bearing damping, stiffness, and friction torque are to be considered, as in equation (1.30), a numerical approach is necessary. The effects could be negligible in a good bearing with proper lubrication and fitment, but in the case of a worn or damaged bearing with little lubrication, or one that has been incorrectly installed with overpressure from press fitting, the effects may be significant. This semi-inverse dynamic approach makes possible advanced qualitative and quantitative analysis for torsional misalignment, and indeed any coupled system. These equations can be used to determine characteristics of the coupling, while other properties will be determined through experimentation.

## 2.5 Eigenfrequencies and Mode Shapes

Natural frequencies for the coupled system can be determined through development of the eigenvalues from the dynamic matrix, a product of the inverse stiffness matrix and mass matrix, or in the case of torsion, the inertia matrix;

$$[\mathbf{D}] = [\mathbf{k}^{-1}][\mathbf{J}] \quad (1.43)$$

Where the stiffness and inertia matrices are;

$$[\mathbf{k}] = \begin{bmatrix} k_\varphi + k_b & -k_\varphi \\ -k_\varphi & k_\varphi \end{bmatrix} \quad (1.44)$$

$$[\mathbf{J}] = \begin{bmatrix} J_r & 0 \\ 0 & J_g \end{bmatrix} \quad (1.45)$$

Determining the eigenfrequencies requires setting up the dynamic matrix in the following frequency form to develop the characteristic equation;

$$\det[\lambda[\mathbf{I}] - [\mathbf{D}]] = 0 \quad (1.46)$$

Yielding four distinct frequencies in the form of a bi-quadratic equation;

$$\omega = \pm \sqrt{\frac{J_g(k_b + k_\varphi) + J_r k_\varphi \pm \sqrt{J_g^2(k_\varphi^2 + 2k_\varphi k_b + k_b^2) + 2J_r J_g k_\varphi(k_\varphi - k_b) + J_r^2 k_\varphi^2}}{2J_r J_g}} \quad (1.47)$$

Matlab® can solve for eigenvalues, however, in order to solve the matrix in (1.46) there needs to be a non-zero value for the bearing torsional stiffness, as a symmetric matrix will yield an error in calculation. Bearing manufacturers do not detail this value and is required that this be determined experimentally due to the many variables that effect the function of the bearing, as detailed in section 2.4. In order to simulate and present a numerical value for this report, an arbitrary value to can be used to solve the system. For the following solutions a value of 10 Nm/rad is assigned to  $k_b$ .

The polar moment for the generator,  $J_g$ , is calculated with the Ø25 mm diameter for the generator shaft excluding any effect of the ABB® motor rotor. For the rotor, the Ø200 mm diameter for the test load is used to calculate  $J_r$ , with the assumption that the mass centre and rotational centres align, for simplicity. The shafts are assumed to

be rigid and as having no effect on the dynamic response of the coupling.

Using the stiffness values shown in sections 3.3.1 and 3.3.2, the natural frequencies for the Lovejoy® and SITEX® couplings are, respectively;

$$\omega_{\text{Lovejoy}} = \left\{ \frac{252}{635 \cdot 10^6} \right\} \frac{\text{rad}}{\text{s}} \quad \omega_{\text{SITEX}} = \left\{ \frac{252}{4.65 \cdot 10^6} \right\} \frac{\text{rad}}{\text{s}}$$

The frequencies obtained can now be used to evaluate the mode shape of the system, by using the distinct  $\lambda$  terms and applying them to the frequency form, and multiplying by an eigenvector,  $\vec{X}$ ;

$$[\lambda_i[\mathbf{I}] - [\mathbf{D}]]\vec{X}^{(i)} = \vec{0} \quad (1.48)$$

Matlab® can solve for eigenvectors, and by using the same assumptions;

$$\vec{X}^{(1,2)} = \left\{ \begin{array}{c} 0.707 - j244 \cdot 10^{-6} \\ 0.707 + j \end{array} \right\}$$

Mode shapes for the torsional vibration of the two couplings are similar, with the above solution valid for both to three significant digits due to the very small values associated. This solution has not included the effect of torsional damping in the system and the solutions only give an estimate of the dynamic response of the coupling, with the aforementioned assumptions.

Determination of the dynamic response is possible through use of the previously detailed semi-inverse dynamics and direct dynamic analysis tools. Valid solutions are only possible once the true stiffness, damping, inertia and moment values have been determined experimentally.

### 3 Determination of Eccentric Mass for Setup 1

The ABB® motor and controller are capable of operating at steady speed to a maximum 1000 r/min [16.67 Hz, 104.71 rad/s]. A suitable operating range is necessary as future experiments may require the addition of instrumentation, including different test mass or additional components. In order to operate both safely and create a suitable shaft speed and subsequent force for spring compression, a maximum speed is chosen at 900 r/min [15 Hz, 94.25 rad/s], to obtain the maximum available torque.

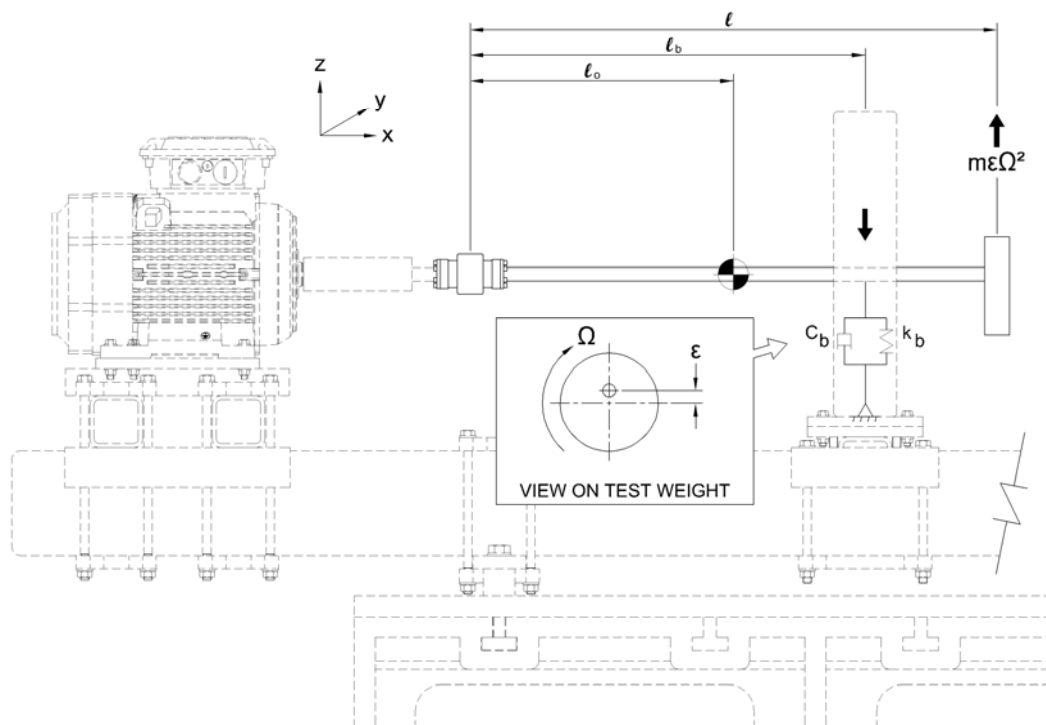


**Figure 20:** *dynamic model for test weight determination.*

Spring motion should not exceed 1.5 mm travel at length corresponding to  $l_b$ , with a tolerance of  $\pm 0.5$  mm to ensure the displacement sensor will not physically contact the steel sensing elements on the frame. The lower limit for shaft speed will be calculated using the same test weight and bearing travel based on sensor minimum sensitivity, at  $10 \mu\text{m}$ .

$$z_{\max} \Big|_{x = l_b} = 1.5 \text{ mm}$$

$$\psi_{\max} = \tan^{-1} \left( \frac{z_{\max} \Big|_{x=l_b}}{l_b} \right)$$

Solving equation (1.20) using the above criteria can be done with Matlab® using the ode45 function, which requires the second order ODE be rewritten in terms of a first order ODE, requiring a new coordinate;

$$X_1 = z \quad X_2 = \dot{z}$$

$$\dot{X}_2 = \ddot{z}$$

Equation (1.20) can now be expressed in terms of the new coordinates. All values are equated to  $\dot{X}_2$  with  $X_1$  and  $X_2$  as subjects, with the constant, as follows;

$$\dot{X}_2 = \frac{F(t, \psi, z)l \cdot l_o - (C_\psi + C_b l_b^2)X_2 - (k_\psi + k_b l_b^2)X_1}{(I_r + m_r l_o^2)} \quad (1.49)$$

The dimension  $X(z)$  refers to the linear distance between the neutral axis and elevation of centre of gravity of the rotor shaft. A geometric relationship exists between the bearing elevation and rotor shaft centroid, therefore a dimensionless ratio using geometric similitude, as shown in figure 21, can be used to scale the solution to

(1.20) in terms of  $z_{\max} \Big|_{x=l_b}$ .

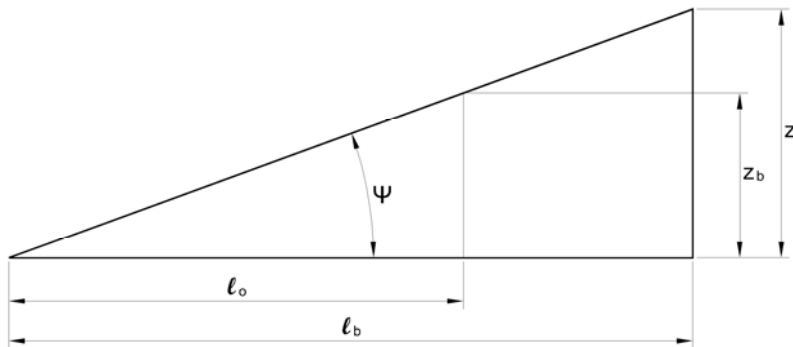


**Figure 21:** illustration showing geometric similitude of system for scaling purposes.

$$\frac{z \Big|_{x=l_o}}{z_{\max} \Big|_{x=l_b}} = \frac{l_o}{l_b} \rightarrow X(z) = z_{\max} \Big|_{x=l_b} \cdot \frac{l_b}{l_o}$$

$$z = \left(\frac{l_b}{l_o}\right) \frac{F(t, \psi, z) l \cdot l_o - (C_\psi + C_b l_b^2) X_2 - (k_\psi + k_b l_b^2) X_1}{(I_r + m_r l_o^2)} \quad (1.50)$$

The above relationship now allows for simulation of the shaft as seen on the z-axis with displacements referred to the bearing, which will be measurable by the displacement sensors installed on the bearing housing.

### 3.1 System Parameters

In order to have a good response from the system with spring displacements within the useable limits on the displacement sensors it is necessary to properly dimension the shaft and eccentric inertial test load. Figure 20 shows the layout of the test bed with motor, bearing housing, coupling, shafts and test load. This is purely an inertial load for the initial testing, so the force will be a function of the mass, eccentricity, and angular velocity.

**Table 1:** parameters for test rig configuration as shown in figure 23.

Parameterisation of Test Rig, Setup 1		
Item	Description	Weight
Shaft	ex-stock Ø25 mm x 1000 mm EN 24T steel bar, $I=1.28 \text{ kgm}^2$	37.7 N
Bearing	FAG 3207-BD 30° angular contact double row ball bearing	4.28 N
Housing	160 x 140 x 40 mm 6061-T6 aluminium	17.56 N
Load	15 kg / 60 kg mass (see section 3.1.3)	N/A
Spring	$4308 \times 10^3 / 8616 \times 10^3 \text{ N/m}$ equivalent stiffness on <b>z</b> -axis	N/A
Damper	assume 0 Ns/m for simulation	N/A
$\omega_{\max}$	900 r/min [15 Hz, 94.2 rad/s]	N/A
$\varepsilon$	25 mm / 60 mm (see section 3.1.3)	N/A
$l$	1000 mm	N/A
$l_o$	500 mm	N/A
$l_b$	750 mm	N/A

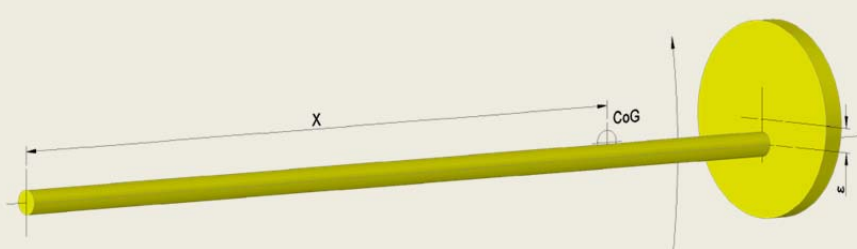
Assumptions are made for ease of calculation, with linear spring coefficient of 4k and 8k, no damping in the system and rigid shafts. Both the rod moment of inertia  $I_r$  and

mass of rod  $m_r$  in this calculation are dependent on the geometry and composition of the rod *and* inertial load.

### 3.1.1 Rotor Shaft Characteristics

An off centre cylindrical mass will create the forces required to shift the bearing, as required for the validation of the model. A Ø200 mm steel cylinder will be added to the end of the rotor shaft, as shown as the illustration in table 2. This outer diameter dimension was chosen due to the wide range and availability of materials which will be suitable as the load. The distance from the mass centre and rotational centre,  $\epsilon$ , is 25 mm or 60 mm, depending on the spring stiffness case. Autocad® models of the rotor shaft and test load were created and the mass properties analysed, with the results presented in table 2.

**Table 2:** rotor dimensions and properties for various masses.

Centre of Gravity and Rotor Polar Moment of Inertia – 25 mm Offset			
			
Load Mass (kg)	Overall Mass Shaft & Rotor (kg)	X - Centre of Mass (mm)	Rotor Moment of Inertia (mm <sup>4</sup> )
5	8.71	773.2	$7.7143 \times 10^{11}$
10	13.56	843.6	$1.3550 \times 10^{12}$
15	18.42	871.7	$1.9148 \times 10^{12}$
20	23.27	883.8	$2.4513 \times 10^{12}$

An iterative approach will be made to find the movement of the spring relative to each different shaft mass and dimensional properties similar to that as shown in table 2, with an assumption that the rotor shaft is considered to be completely rigid for ease of calculation.

### 3.1.2 Evaluation of Bearing Housing Spring Deflection

Four cases of eccentric test weights on the rotor are simulated to determine displacement of the spring at the systems 15 Hz upper limit using the known parameters and rotor specifications system from table 2.

The ODE describing the shaft angle and spring displacement has focus on a single axis; however, this is a multi-degree of freedom system with a time dependent input force. The time function on the test mass can be approximated by;

$$F(t, \psi, z) \approx m\epsilon\Omega^2 \quad (1.51)$$

Frequency of vibration for the shaft angle and rotor angular velocity are independent of one another, but at a given rotor speed the force function will result in constant magnitude vector rotating about the rotor axis. Approximating this requires some assumptions be made, such as the motion of the shaft angle on the  $z$  axis is sinusoidal and the full force vector from the eccentricity align with the peaks of spring travel. The following diagram shows the relationship between shaft angle and force.

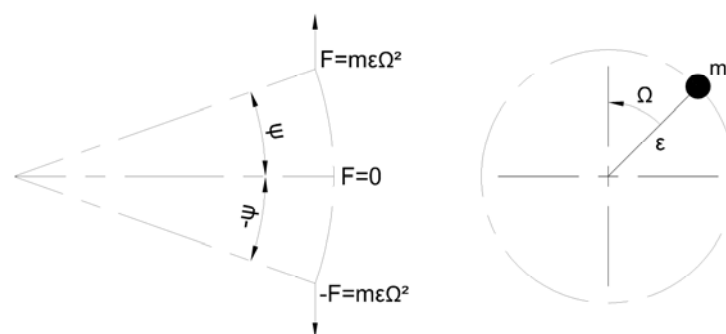


**Figure 22:** *forcing function approximation with shaft z-axis.*

$$F(t, \psi, z) \approx F \sin(\Omega t) \quad (1.52)$$

The force function is analogous to a pendulum, with peak forces at end of travel, which as stated above, are assumed to be mutual with the maximum angular positions of the shaft. The force is a constant due to constant angular velocity, and is multiplied by the product of periodic trigonometric function, with limits at 0 and F-max. This can be written as shown in equation (1.52) which will be useable in Matlab® for an ODE45 function call as the forcing function.

In section 1.15.2 the characteristics of stiffness for the frame were detailed, explaining

the possibility of there being two stiffness cases on the axis of interest, either 4k or 8k, dependent on pre-loading. It is therefore required to test the response of the rotor and bearing housing spring displacement in both cases.

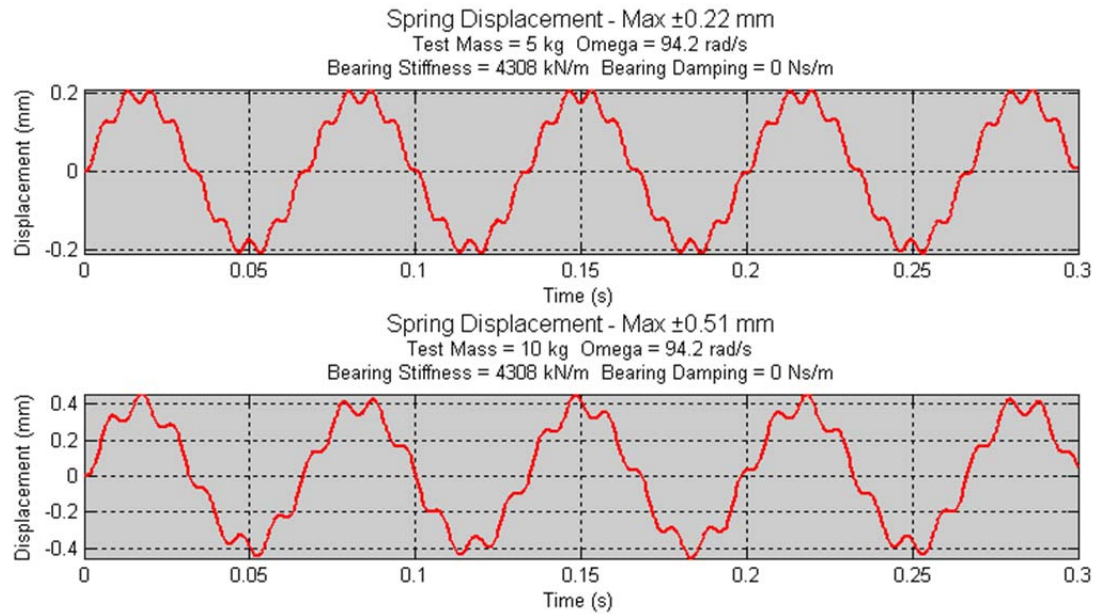


**Figure 23:** spring deflection with 5 kg and 10 kg test weights, 25 mm eccentricity.

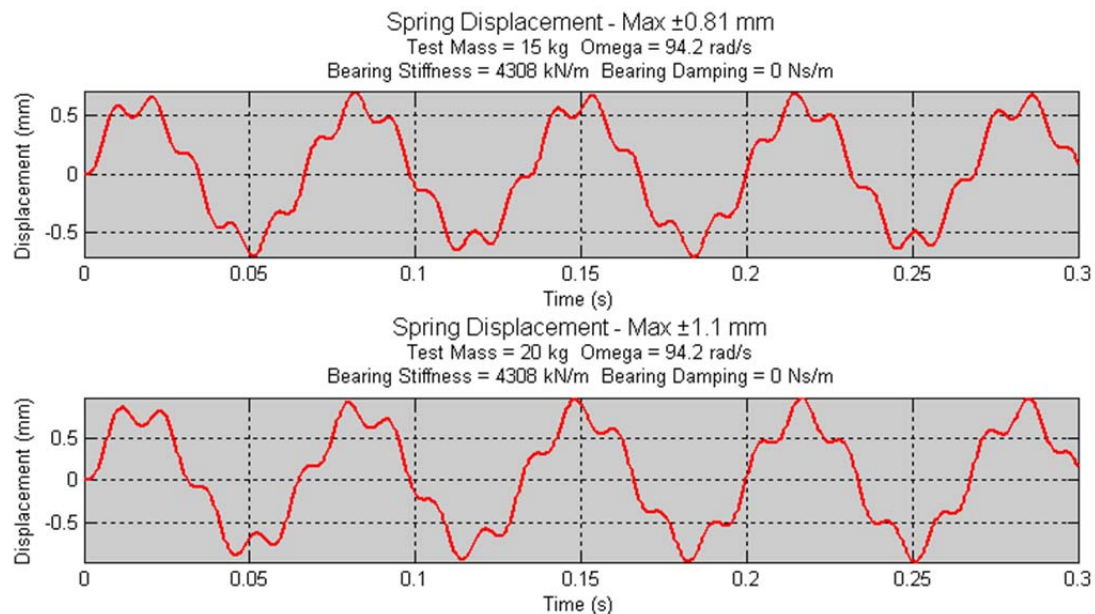


**Figure 24:** spring deflection with 15 kg and 20 kg test weights, 25 mm eccentricity.

For the case of the 4k spring stiffness, the eccentricity distance, that being the linear distance between rotational centre and mass centre is 25 mm. With the 8k stiffness scenario, a distance of 60 mm was chosen, with the same masses. For the initial simulation, the value of the rotor moment of inertia has been kept constant for both

offsets. Results of the Matlab® simulations for the 4k stiffness and various test weights are detailed graphically in figures 23 and 24. Figures 25 and 26 show the results for the 8k stiffness.

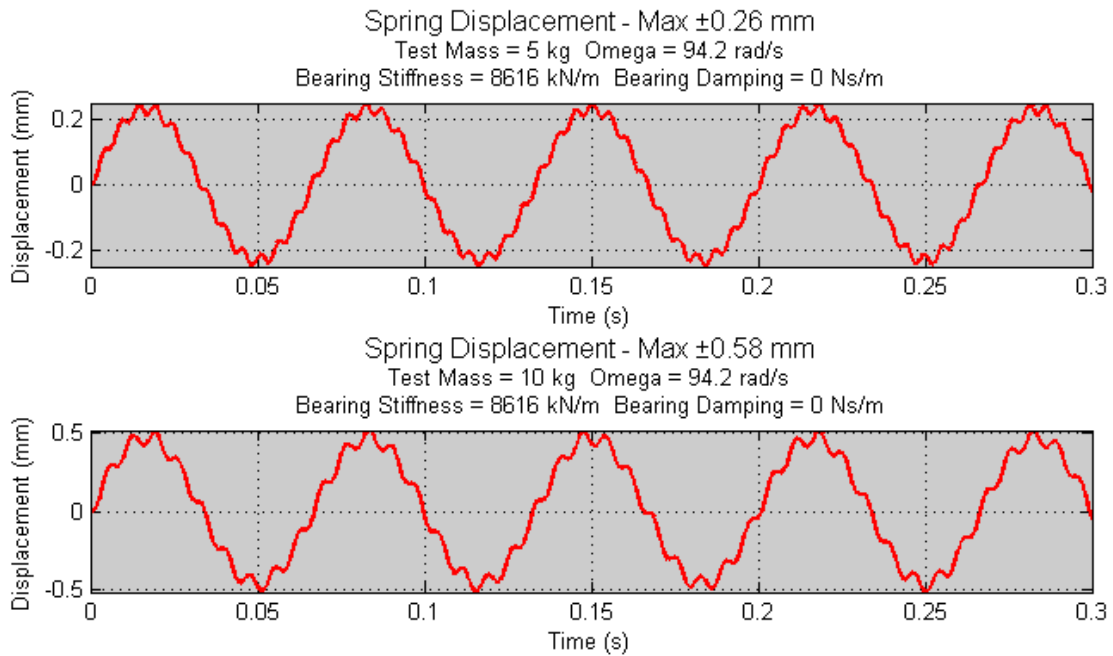


**Figure 25:** spring deflection with 5 kg and 10 kg test weights, 60 mm eccentricity.

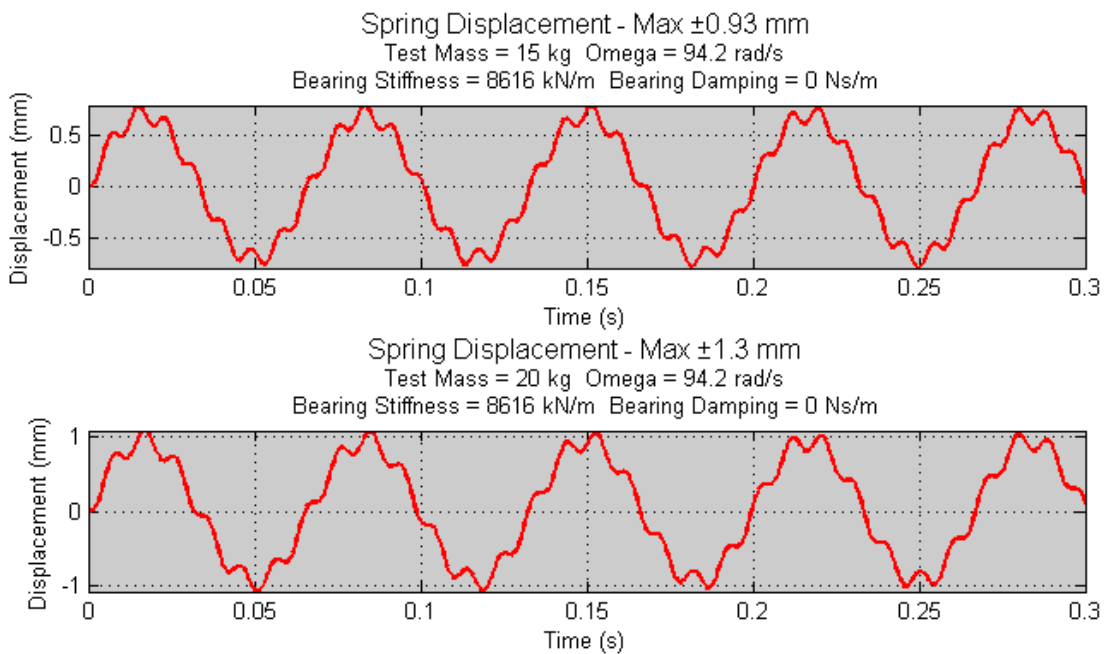


**Figure 26:** spring deflection with 15 kg and 20 kg test weights, 60 mm eccentricity.

Spring motions for the heavier two weights are in the region of  $1.5 \text{ mm} \pm 0.5 \text{ mm}$  as required by the project build. Results on figure 24 show the best candidate weights to be 15 kg and 20 kg for the 4k stiffness case. This assumed force function may not work in the real model, so careful testing is a necessity for safety of personnel and equipment.

As with the smaller spring stiffness case, spring motions for the heavier two weights and 8k springs are in the region of  $1.5 \text{ mm} \pm 0.5 \text{ mm}$ . Results on figure 26 show the best candidate weights to be the two heavier ones (ie, 8k). These results serve as an approximation to the real system response, requiring thorough testing experimentally to choose the best candidate, based on the dimensions used in the simulations.

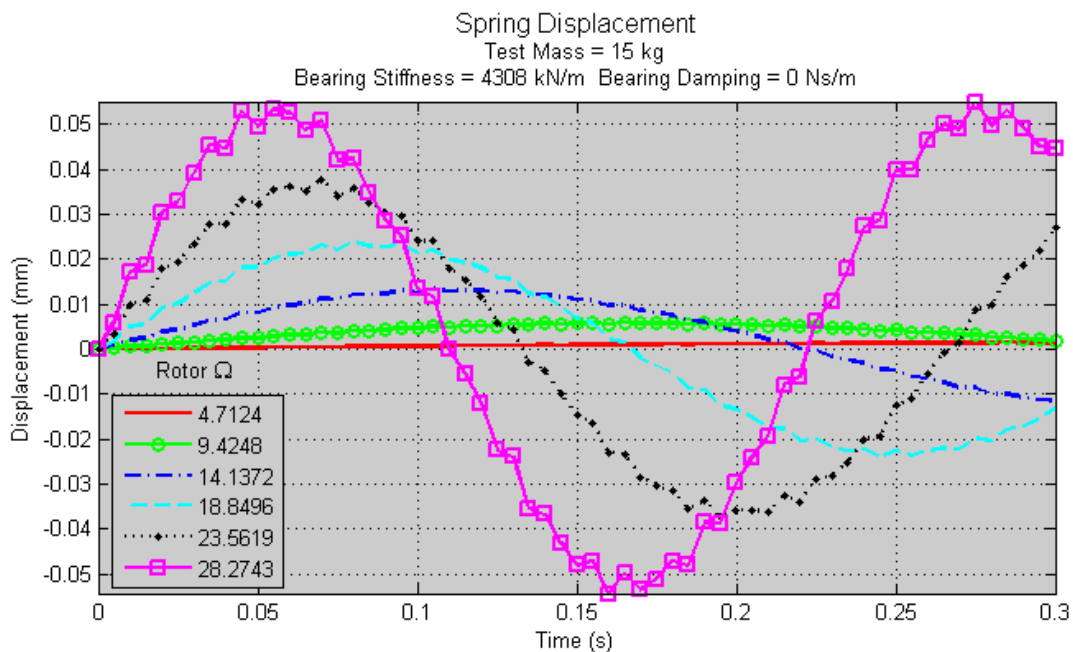


**Figure 27:** *spring deflection over range of frequencies for 15 kg, 25mm eccentricity.*

To evaluate the lower speed limit corresponding to the limit of displacement sensor range at  $10 \mu\text{m}$ , an iterative algorithm has been developed to find the optimal shaft speed, based on spring deflection over a range of fractions of the design speed of 15 Hz [94.4 rad/s]. Force derived from centripetal motion on the eccentric test weight will diminish by the square of the speed.

Determination of the spring displacement will be made by testing selected test weights at predetermined speed intervals, using the previous equation. This will establish a lower speed limit for experimentation.

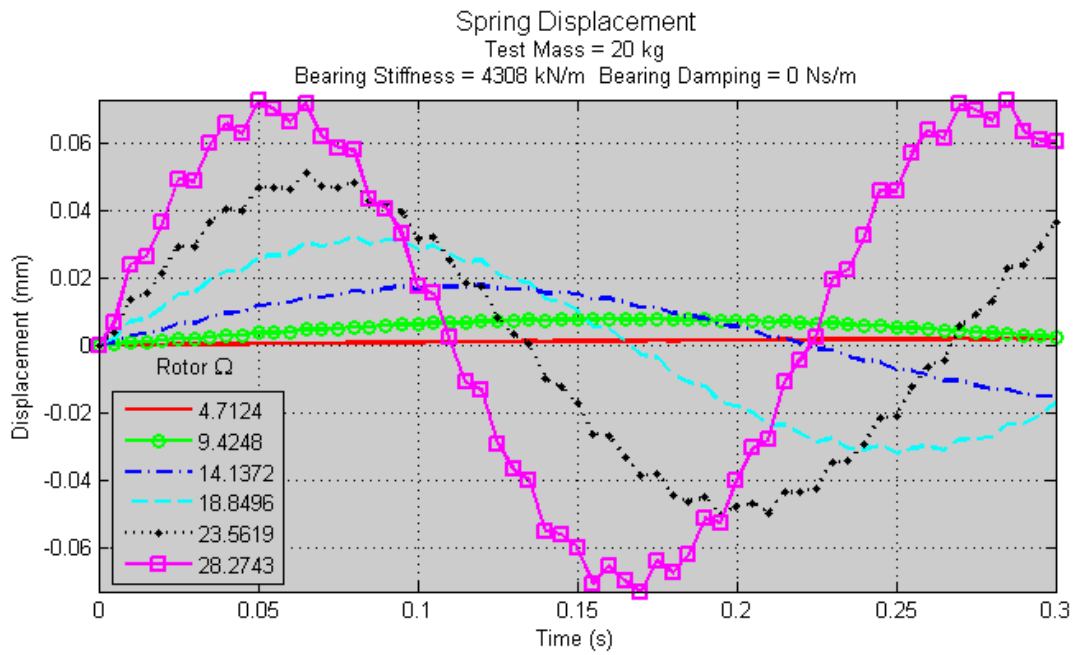


**Figure 28:** spring deflection over range of frequencies for 20 kg, 25mm eccentricity.

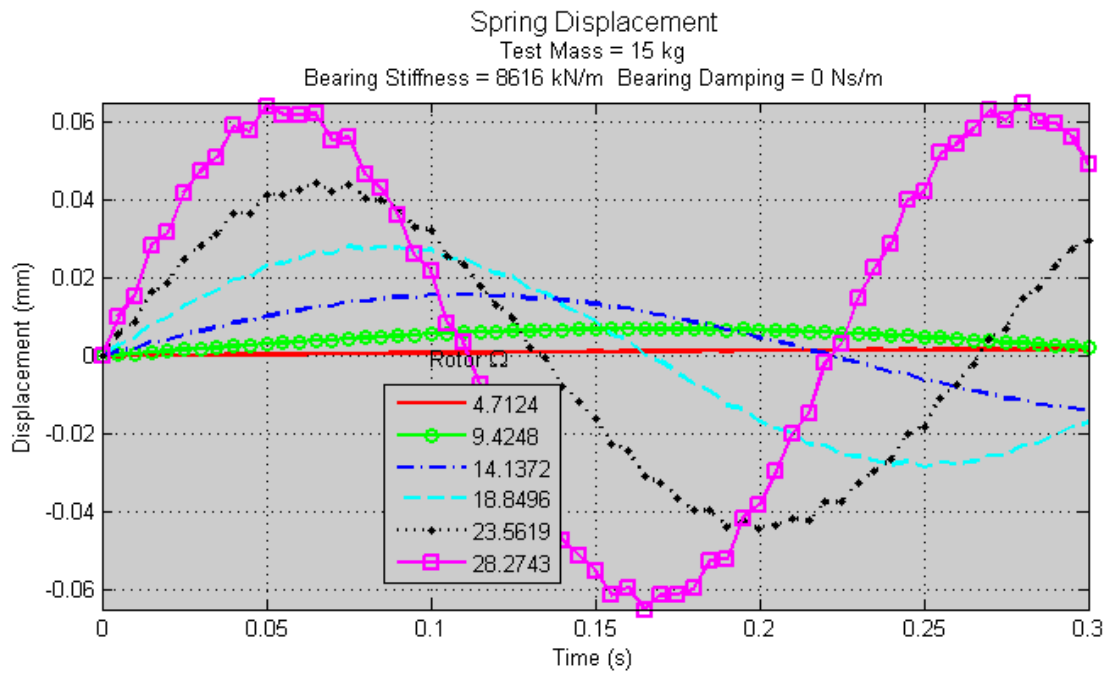


**Figure 29:** spring deflection over range of frequencies for 15 kg, 60 mm eccentricity.

A range of speeds with the 15 kg and 20 kg test weights are chosen to find the optimal lower speed limit, with speeds from 5% to 30% of the maximum 15 Hz. Results are shown in figures 27 and 28 for the 4k stiffness case, and figures 29 and 30 for the 8k stiffness case. From these graphs limits a shaft speed range can be estimated for the different experimental test weights and spring stiffness cases.

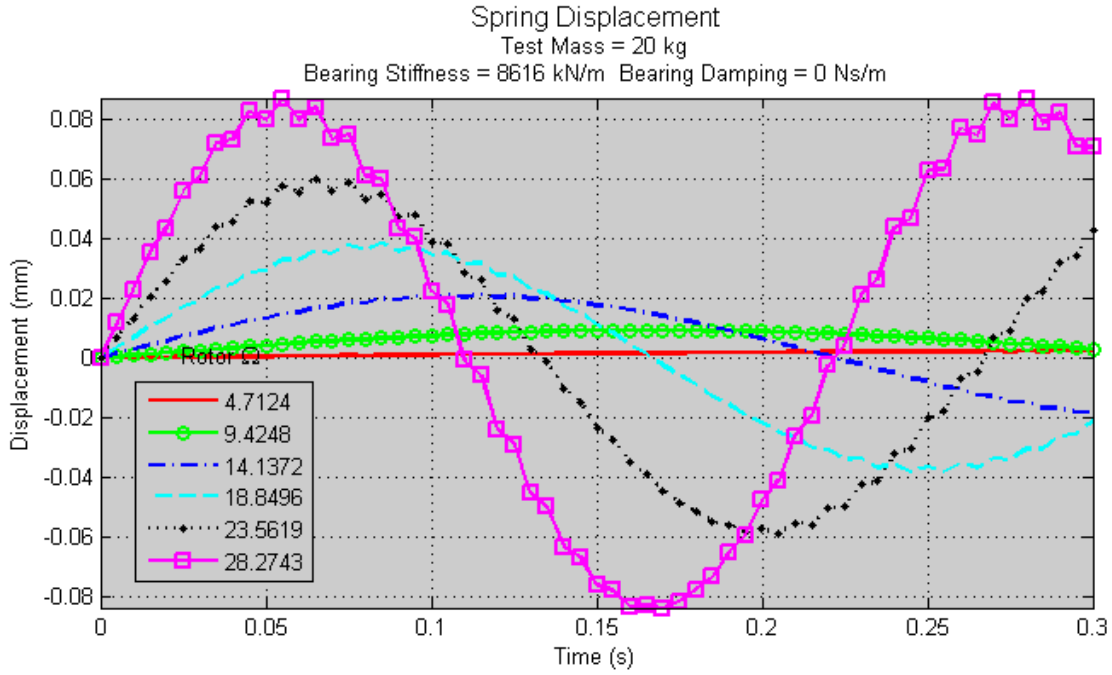


**Figure 30:** spring deflection over range of frequencies for 20 kg, 60 mm eccentricity.

The following set of operational limits are presented for the various cases, first for the 4k stiffness case with 25 mm shaft load eccentricity;

$$12.2 < \Omega \Big|_{m = 15 \text{ kg}, \varepsilon = 25 \text{ mm}} < 94.2 \text{ rad/s} \quad (1.53)$$

$$9.9 < \Omega \Big|_{m = 20 \text{ kg}, \varepsilon = 25 \text{ mm}} < 94.2 \text{ rad/s} \quad (1.54)$$

And for the 8k stiffness case with 60 mm shaft load eccentricity;

$$11.0 < \Omega \Big|_{m = 15 \text{ kg}, \varepsilon = 60 \text{ mm}} < 94.2 \text{ rad/s} \quad (1.55)$$

$$9.4 < \Omega \Big|_{m = 20 \text{ kg}, \varepsilon = 60 \text{ mm}} < 94.2 \text{ rad/s} \quad (1.56)$$

As previously noted in section 1.15.2, the event of non-linearity which can arise when the pre-loaded case spring travel is exceeded, will garner different results from what has been simulated here. This is an area that would require more study, to include the effect of shaft bending which has also not been taken into consideration for this report.

### 3.2 Evaluation of Torsional Vibration

The system of equations of motion for the generator and rotor shaft torque angles can be evaluated analytically to determine Eigen-frequencies and mode shapes, and numerically through Matlab®. Torsional displacement as developed in equations (1.18) and (1.19) are presented in matrix format;

$$\begin{aligned} \begin{bmatrix} J_r & 0 \\ 0 & J_g \end{bmatrix} \begin{Bmatrix} \ddot{\varphi}_r \\ \ddot{\varphi}_g \end{Bmatrix} + \begin{bmatrix} C_\varphi + C_b & -C_\varphi \\ -C_\varphi & C_\varphi \end{bmatrix} \begin{Bmatrix} \dot{\varphi}_r \\ \dot{\varphi}_g \end{Bmatrix} + \begin{bmatrix} k_\varphi + k_b & -k_\varphi \\ -k_\varphi & k_\varphi \end{bmatrix} \begin{Bmatrix} \varphi_r \\ \varphi_g \end{Bmatrix} \\ = \begin{Bmatrix} -M_r(t, \varphi_r) \\ M_g(t, \varphi_g) \end{Bmatrix} \end{aligned} \quad (1.57)$$

Matlab® can numerically solve for a system of equations. In order to present the data in a form that can be utilised in Matlab®, the equation coordinates must be re-written in terms of first order ODE's.

When coding for Matlab® it is necessary to format the equations in state space form with the system of equations expressed in a vector of first order differentials, and a second vector containing the initial conditions;

$$\begin{Bmatrix} \dot{X}_1 \\ \dot{X}_2 \\ \dot{X}_3 \\ \dot{X}_4 \end{Bmatrix} = \begin{Bmatrix} X_1 \\ X_2 \\ \frac{C_\varphi(X_4 - X_3) - C_b X_3 + k_\varphi(X_2 - X_1) - k_b X_1 - M_r(t, \varphi_r)}{J_r} \\ \frac{C_\varphi(\dot{X}_3 - \dot{X}_4) + k_\varphi(X_1 - X_2) + M_g(t, \varphi_g)}{J_g} \end{Bmatrix} \quad (1.58)$$

$$\begin{Bmatrix} X_1(0) \\ X_2(0) \\ X_3(0) \\ X_4(0) \end{Bmatrix} = \begin{Bmatrix} 0 \\ 0 \\ 0 \\ 0 \end{Bmatrix} \quad (1.59)$$

For state modelling, the initial conditions will be based on the system at rest, that is with no initial torsional displacement and no initial velocities, as shown in the

### 3.3 Simulation of Torsional Vibration

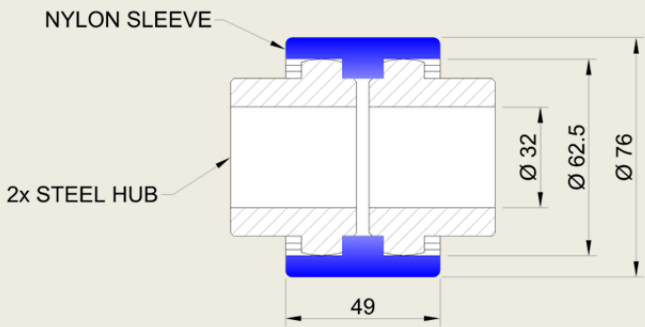
Torsional stiffness can be estimated for the coupling using the geometry and material properties. Torsional spring coefficient, which is analogous to the linear spring

coefficient, can be solved, in units  $\frac{Nm}{rad}$ ;

$$k_l = \frac{AE}{l} \rightarrow k_t = \frac{JG}{l\phi} = \frac{\pi r^4 E}{4l(1 + \nu)\phi} \quad (1.60)$$

### 3.3.1 Coupling 1

**Table 3:** parameters for Sitex® coupling.

Parameters for SITEX® #5-32 Sleeve		
		
Item	Description	Value
Sleeve	Polyamide (nylon)	-
	Young's modulus [18]	4 GPa
	Poisson ratio	0.4

The first coupling is from SITEX®, which consists of two 40-toothed steel hubs which are coupled with a nylon sleeve, with mating slots for the hub teeth. This sleeve is designed for low torque applications and will be used for the first experiment using the eccentric mass as it will see very low torques on the shafts. Torsional stiffness for the SITEX® coupling is estimated by the geometry of the polyamide (nylon) sleeve, and its material properties, as shown in table 3, and the following formulas.

$$J_c = \frac{\pi(r_o^4 - r_i^4)}{2} \quad (1.61)$$

Polar moment for the coupling is  $1.78 \times 10^{-6} \text{ m}^4$ .

$$G_c = \frac{E}{2(1 + \nu)} \quad (1.62)$$

Shear modulus for the coupling, using the upper value estimate for Young's modulus is 1.43 GPa. Torsional stiffness using the worked polar moment and shear modulus, the length of the sleeve and formula (1.60) is therefore estimated as 829 kNm/rad.

### 3.3.2 Coupling 2

**Table 4:** parameters for Lovejoy Inc® coupling.

Parameters for Lovejoy Inc® L-110 Coupling		
Item	Description	Value
Spider	Urethane	-
	Young's modulus	85 MPa
	Shear modulus	28.3 MPa
	Poisson ratio	0.5

The second coupling is from Lovejoy Inc® consists of two 3-toothed steel hubs between which rests a urethane spider. This sleeve is a suitable to high torques and will be used for the parallel spur gear experiments, and others involving coupled motor and generation arrangements. This coupling operates in shear within the ring portion, and linearly on the spider legs.

$$S_D = 100 - \frac{20(-78.188 + \sqrt{6113.36 + 781.88E})}{E} \quad (1.63)$$

The compressible cross sectional area of a leg is 409 mm<sup>2</sup>, and the mean radius on the area is 31.1 mm. The polar moment for the inner ring section is 3.39x10<sup>-6</sup> m<sup>4</sup>. Young's modulus was not readily available on the spider; however, the manufacturer specifies a Shore hardness of 55D for the spider. Using a conversion factor derived by Qi, Joyce and Boyce [19], the Young's modulus is calculable with the following

implicit relationship to Shore D hardness from their empirically derived formula, with the result expressed in MPa;

The torsional stiffness works in parallel with the linear stiffness, where the linear stiffness can be approximated as a torsional stiffness through the product of the linear force and mean radius, expressed as a function of the torque angle; small angles are assumed and six legs on the spider are considered. Torsional stiffness is estimated at 4.97 kNm/rad, and linear stiffness at 1801 kN/m.

$$k_{eq} = k_t + 6k_l(r^2\varphi) \quad (1.64)$$

Equivalent torsional stiffness of coupling is 4.97 kNm/rad plus 10.5 kNm per rad.

### 3.3.3 Torsional Vibration Simulations

#### 3.3.3.1 SITEX® Coupling

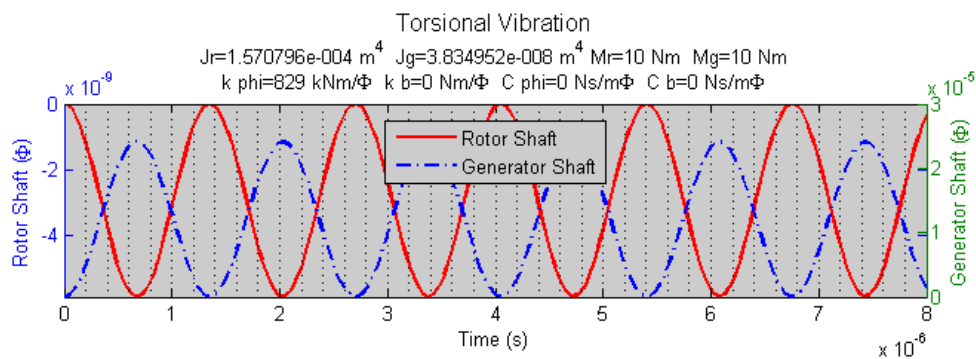


Figure 31: graph of Sitex® coupling torsional vibration, 10 Nm torque couple.

#### 3.3.3.2 Lovejoy Inc® Coupling

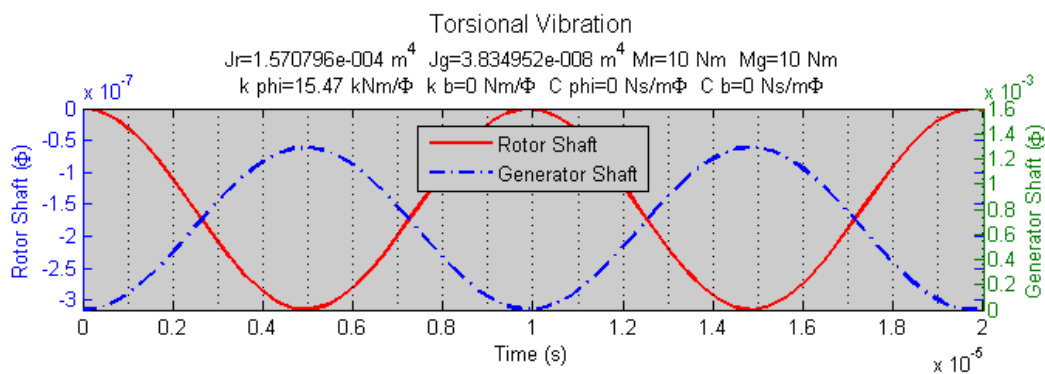


Figure 32: graph of Lovejoy Inc® coupling torsional vibration, 10 Nm torque couple.

These values are used in the above simulations with some assumptions: rigid generator and rotor shaft, no coupling torsional damping, no bearing torsional stiffness or damping, equal and opposing moments (torques) on shafts.

## 4 Frame Dynamics

Analysis of the frame is to be completed to ensure that the exciting frequencies of the motor and load do not approach resonance. Figure 33 shows the setup for the frame, assuming no self weight on the beam itself.

### 4.1 Test Frame Dynamic Analysis

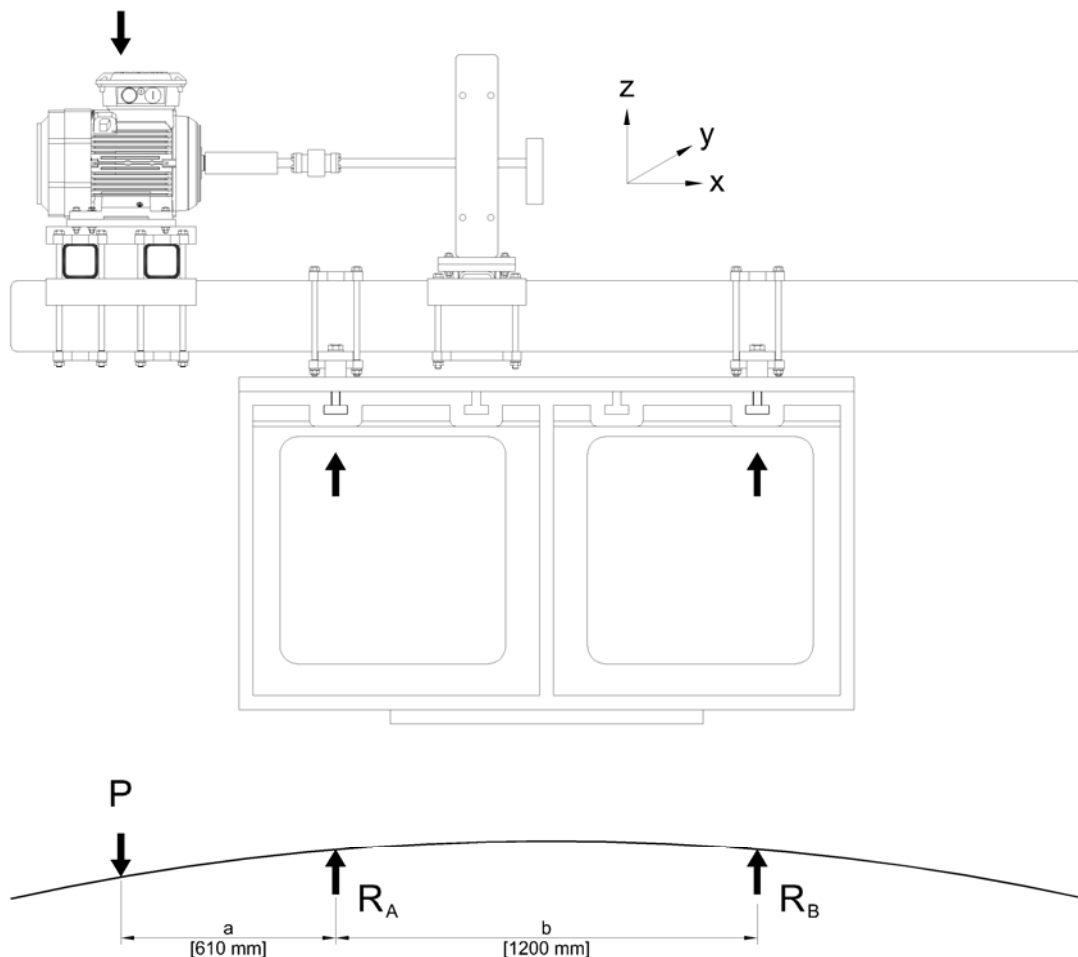


**Figure 33:** illustration of maximum load case on test frame beam.

The formulaic solution to deflection for the beam is shown in equation (1.65) and takes into consideration of the load consisting of the motor, motor mounting system and fasteners. This is summed in table 5. It is assumed that the fastening system is rigid at  $R_A$  and  $R_B$ , the cross section of the beam is homologous throughout its length, and the load is taken from the worst case example, which is at the limit of adjustability way from the centre of the table. The load case for the beam is shown in Figure 33.

Deflection of the beam at load (P);

$$z = \frac{Pa^2}{6EI}(a + b) \quad (1.65)$$

Equivalent stiffness of beam at load;

$$k_{eq} = \frac{P}{z} = \frac{6EI}{a^2}(a + b)^{-1} \quad (1.66)$$

Natural frequency of beam at load;

$$\omega_n = \sqrt{\frac{k_{eq}}{m}} \quad (1.67)$$

BS EN 10025 S275 steel has a Young's Modulus of 205 GPa, with a yield stress of 275 MPa. The cross sectional moment of inertia for the beam ( $I_{yy}$ ) was determined to be  $1.559 \times 10^{-3} \text{ m}^4$  by use of AutoCad® and its mass property inquiry function, with complete results of section property inquiry shown in figure 34.

**Table 5:** *table of masses for main frame analysis.*

Motor	127 kg
Support Frame	54 kg
Mount	29 kg
Clamps and fasteners	15 kg
	225 kg

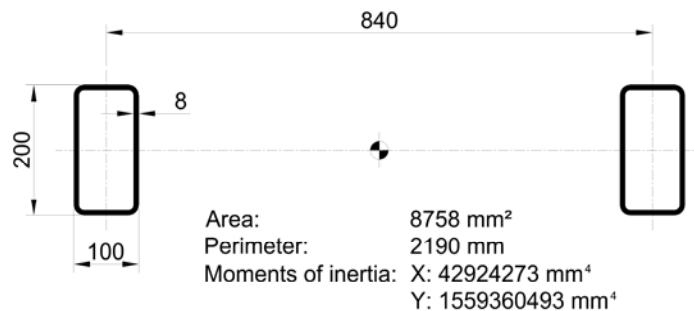


**Figure 34:** *properties of test frame section.*

When calculated through, the deflection in the beam at load is negligible at  $775 \times 10^{-9}$  m. Calculating the equivalent stiffness using formula (1.65) works out to  $2.849 \times 10^9$

N/m. The natural frequency of the beam at load is therefore calculated to be 3558 rad/s, or 566 Hz, using formula (1.67).

## 4.2 Test Frame Stress Analysis

In addition to the dynamic analysis of the test frame, the stress due to loading in maximum condition must be determined to ensure that loading will not be unsafe.

Stress at maximum fibre;

$$\sigma = \frac{Mz}{I} \quad (1.68)$$

Using geometry and maximum case loading, with the cantilever arrangement as shown in figure 33, from the load (P) through to the left support ( $R_A$ ), the moment is  $1.346 \times 10^3$  Nm. The distance from neutral axis to maximum fibre is  $\pm 100$  mm. The moment of inertia ( $I_{yy}$ ) remains the same at  $1.559 \times 10^{-3} \text{ m}^4$ . Stress in the test frame beam at maximum load case is therefore calculated to be  $86.3 \text{ kN/m}^2$  which is well below the  $275 \text{ MN/m}^2$  yield rating of the steel, and safe to support the load in all cases.

## 4.3 Support Frame Dynamics

In addition to the main test frame, the separate motor support frame system should be analysed for dynamic response, with the loading shown in figure 35.

Properties of the steel are consistent throughout the framework, with Young's modulus and yield stress constant. The cross sectional moment of inertia for the beam ( $I_{yy}$ ) is  $82.4 \times 10^{-6} \text{ m}^4$ , using methods as detailed in the previous frame section analysis.

Deflection of the beam at load (P);

$$z = \frac{Pa^3}{48EI} \quad (1.69)$$

Equivalent stiffness of beam at load;

$$k_{eq} = \frac{P}{z} = \frac{48EI}{a^3} \quad (1.70)$$

Natural frequency of beam at load is calculated in the same manner as equation (1.67)

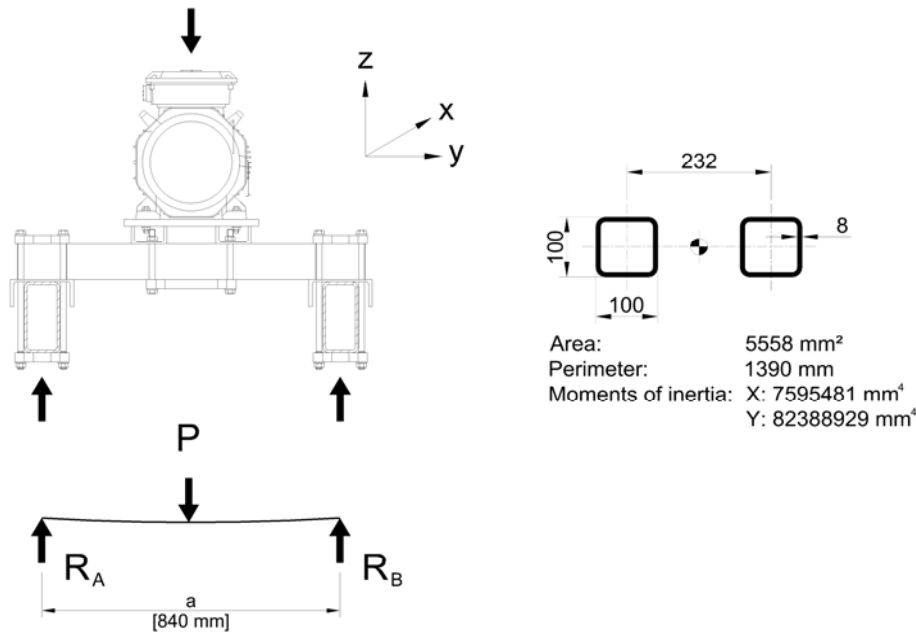


**Figure 35:** illustration of maximum load case on motor support beam and section properties.

When calculated through, the deflection in the beam at load is  $1.226 \times 10^{-6}$  m. Calculating the equivalent stiffness using formula (1.70) works out to  $1.368 \times 10^9$  N/m. The natural frequency of the beam at load is therefore calculated to be 2828 rad/s, or 450 Hz.

**Table 6:** table of masses for support frame analysis.

Motor	127 kg
Mount	29 kg
Clamps and fasteners	15 kg
	171 kg

#### 4.4 Support Frame Stress Analysis

Using geometry and maximum case loading, with the simply supported mid-point load arrangement as shown in Figure 35, from the load (P) through to the left support ( $R_A$ ), the moment is  $1.409 \times 10^3$  Nm. The distance from neutral axis to maximum fibre is  $\pm 50$  mm. The moment of inertia ( $I_{yy}$ ) remains the same at  $82.4 \times 10^{-6}$  m<sup>4</sup>. Stress in the motor support beam at maximum load case is therefore calculated to be  $855$  kN/m<sup>2</sup>, well below the  $275$  MN/m<sup>2</sup> yield rating of the steel, and is to be considered safe to support the load in all cases.

## 5 Results

The design of the test rig has been completed to what can be considered an initial phase. Structural steel components, fasteners, motors and controllers, and sensors are all specified, with most delivered to the Vibration and Smart Structures Laboratory in Chalmers University of Technology. There are many drawings and schematics, as well as calculations which parameterise and verify this stage of engineering design.

The design process followed the concepts as detailed in this report, with an overview on the engineering, mathematical, and computational models created. Examination of the resultant dynamics of the rotor shaft and test load through simulation serves to verify the engineering and mathematical model. Further studies including more advanced simulations along with experimental data will serve as the basis for validation of the engineering design.

The main concepts for test rig criteria have been captured, including adjustability in terms of introduced forces and a modular and upgradeable form. Simulations of various load cases for the rotor shaft inertial load model have been completed, based on initial conditions and physical constraints from the motor and generalised setup. These results will be manifested into a working system of components where the initial testing of the rig can take place.

Initial fitting of components the test rig showed no deficiencies, however, this is to be considered an ongoing and evolutionary process. Final design considerations will be made once the test rig is fully functional, with all sensors fitted, safety systems realised, and real time data acquired. In addition to the original specifications, extra measures to prevent electro-magnetic contamination passing from the motor and controller have been made to reduce noise in sensors have been considered. Fitting of the electrical motors and controllers will require a significant amount of specialist labour, as this is a 400 V AC, 3-phase power source with potentially large currents, up to 30 amps.

Dynamic calculations made for the test rig frame show that operation of the test rig at the design frequency of 15 Hz will not be an issue, in respect to resonance frequencies of the frame sub-components, which is sufficiently stiff for the proposed experiments. Stress analysis shows that the frame is mechanically strong enough for the proposed motors and ancillary equipment.

## 6 Conclusions and Outlook

Initial concepts for the test rig were captured by analysis of research and technical papers, published by industry and academia. In what can be considered the archetype of wind turbine test rigs at the NREL, many key ideas were captured through analysis of their extensive technical literature base. Additionally, concepts and ideas from similar projects were examined by the author and Chalmers design team in order to integrate into the design. Several key areas of operation and interest were singled out from the large literary base which would be integrated into the design as detailed in this report.

Development of the test rig from conception to fabrication involved the efforts of many people and academic disciplines. Although this project can be considered mainly mechanical in its operation and required outputs, there is a significant amount of electrical work involved through prime mover excitation and fitted sensors. Within the mechanical engineering spectrum, fields of study such as dynamics, statics, and stress analysis have been utilised for design and verification. On the electrical side, motion control, transducers, and data acquisition systems have been specified, requiring knowledge of 3-phase induction machines, instrumentation, and data acquisition, all of which use either AC or DC voltages. Design also involved the use of engineering software packages. Concepts were sketched on paper and transferred into 2D and 3D CAD models, using AutoCad®. Mathematical simulations for many aspects of the test rig were completed using Matlab®.

By utilising the EMC modelling techniques as detailed in this report, the process of design using this system has been a success. In the mathematical model, techniques such as Lagrange-Euler and Newton Method were used to formulate suitable models describing the dynamic response to the test rig. These models were then evaluated numerically with Matlab® and by hand calculation to create within the computational modelling stage, serving as verification to the mathematical models.

This design algorithm has been successfully implemented and will be the basis for ongoing studies in the test rig, for both future iterations and more detailed analysis of the current engineering model. This report will serve to educate the reader on the aspects of the test rig, areas of interest to the energy industry, and grant a more insightful view onto what parameters are of importance to the engineering and

reliability fields in respect to wind energy and drive train systems. The test rig will continue to be put together by both Chalmers staff and research students. The initial construction will require the completion of setup 1, including installation of all instrumentation and data acquisition systems. Select drawings are available in the appendix which shows the general arrangements of test setup 1 and 2, shaft connectivity, 3-phase power requirements as well as a proposed sensor schematic for the current and proposed future test rig setups.

The initial test loads for the self exciting case have been determined and it is recommended that the first trials use the 15 kg test mass, with a very slow ramp up to maximum speed. This follows for the 20 kg test mass as well. Data from the displacement sensors is to be checked against the simulated values for verification of the model for both masses. Additionally, the initial setup should be scrutinised for transmitted vibration through the frame, to ensure that the modelling and calculated results of frame dynamics. Additional displacement sensors or accelerometers on the frame can be used to detect vibration. This can be accomplished by setting a magnetic base to the test bed table to hold the displacement sensor, or alternatively, an accelerometer can be fitted directly to the frame at the most convenient point.

Chalmers and the design team have put a lot of effort and time into construction of the rig and plan to introduce this test rig in 2014 to its students and partnerships. Final construction of the mechanical and electrical components and functional testing will be completed with the goal of integrating the SKF® WindCon™ conditioning monitoring suite into the test rig. Integrating all this hardware and software will require extensive efforts on the part of future students, researchers and Chalmers staff.

A professional attitude towards workmanship was upheld throughout the design and report writing process. Proper record keeping was adhered to through the use of logbooks, regular team meetings and several informative seminars put on by the author. Chalmers and its industry partners have a significant level of interest in this project, as the condition monitoring and reliability study of wind turbines is a hot topic within the energy industry at the time of writing. Ultimately, the test rig will be able to simulate conditions faced by contemporary wind turbine drive trains with the desired outcome being the ability to detect, prevent, and predict failure.

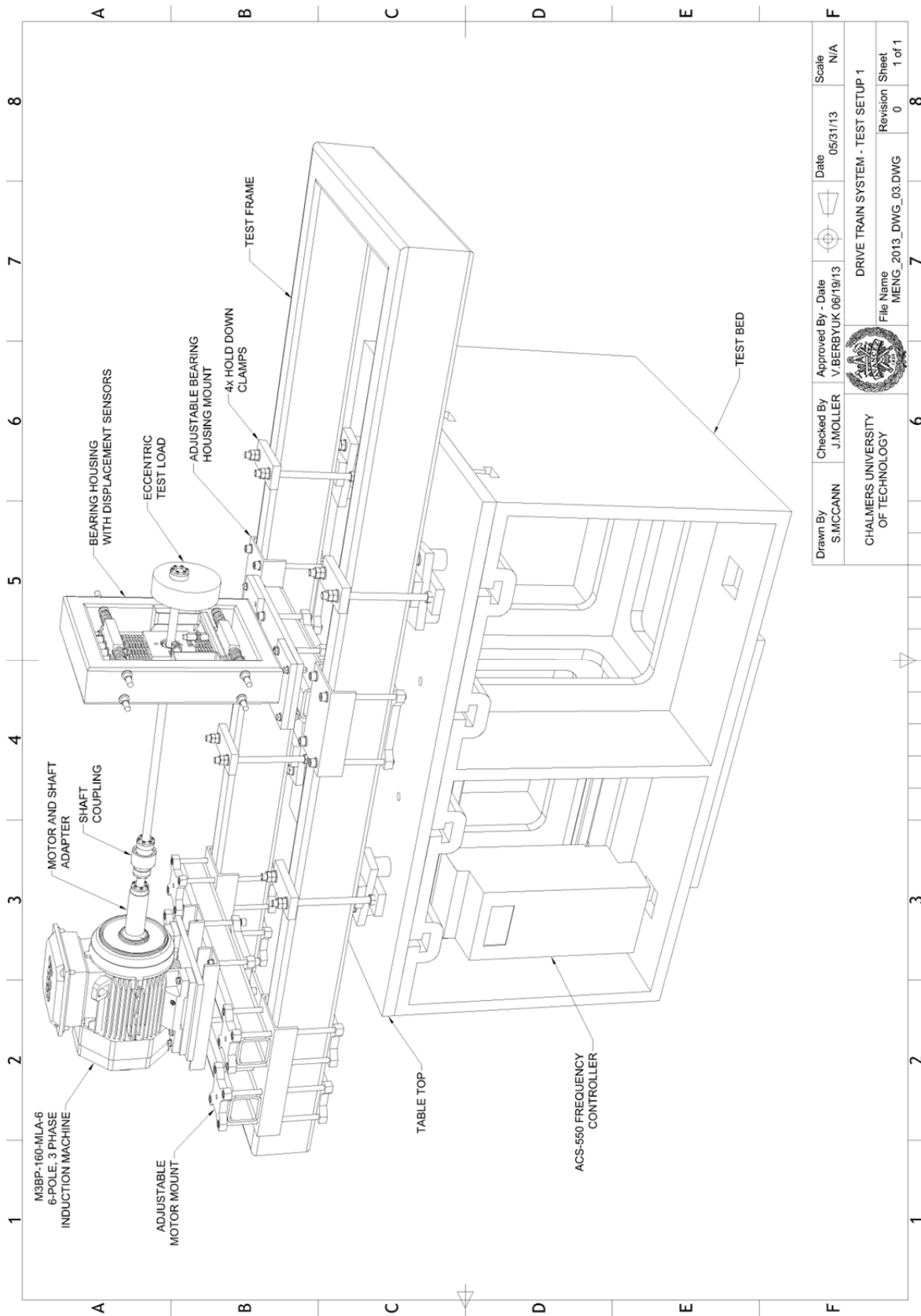
## 7 References

- [1] Puigcorbe, Jordi, and Alexis de-Beaumont . "Wind Turbine Gearbox Reliability." *Renewable Energy World*. 03 Jun 2010: n. page. Web. 22 Mar. 2013. <<http://www.renewableenergyworld.com/rea/news/article/2010/06/wind-turbine-gearbox-reliability>>.
- [2] Li, Yaoyu, Xin Wu, and Zhongzhou Yang. *A Review of Recent Advances in Wind Turbine Condition Monitoring and Fault Diagnosis*. Diss. Ed. Bin Lu. University of Wisconsin, 2009. N.p.: n.p., n.d. *IEEE Explore Digital Library*. Web. 20 Mar. 2013.
- [3] Tegan, S, M Hand, et al. United States. National Renewable Energy Laboratory. *2010 Cost of Wind Energy Review*. Denver: NREL, 2012. Web.
- [4] D. Ancona, J. McVeigh, "Wind Turbines – Materials and Manufacturing Fact Sheet," Princeton Energy Resources LLC, 31 Aug. 2001, pp. 2.
- [5] Butterfield, S, S Sheng, et al. United States. National Renewable Energy Laboratory. *Wind Turbine Drivetrain Condition Monitoring During GRC Phase 1 and Phase 2 Testing*. Colorado: , 2011. Web.
- [6] "NREL & Samsung Obtain Decades of Wind Power Data in Two Months of Testing." *Wind Power*. Alternative Energy Newswire, 19 May 2010. Web. 14 May 2013. <<http://www.alternativeenergynewswire.com/nrel-samsung-obtain-decades-of-wind-power-data-in-two-months-of-testing>>.
- [7] Peeters, Joris, Dirk Leimann, and et al. "First results of Hansen's 13 MW test facility for wind turbine gearboxes." The European Wind Energy Association. Hansen Transmission, n.d. Web. 7 Jun 2013.
- [8] Helsen, Jan, Frederik Vanhollebeke, et al. "Multibody modelling of varying complexity for modal behaviour analysis of wind turbine gearboxes." *Renewable Energy*. 36. (2011): pp. 3100. Print.
- [9] Sheng, S, M McDade, and R Errichello. United States. National Renewable Energy Laboratory. *Wind Turbine Gearbox Failure Modes – A Brief*. Colorado: , 2011. Web.
- [10] "A research centre for the design and production of wind turbines." *Swedish Wind Power Technology Center*. Chalmers, 15 Oct 2010. Web. 7 Jun 2013. <<http://www.chalmers.se/ee/swptc-en/about-us>>.
- [11] Baldo, F. *Modelling of Load Interfaces for a Drive Train of a Wind Turbine*. MSc thesis. Chalmers University of Technology, 2012. Chalmers Reproservice, 2012. Print.

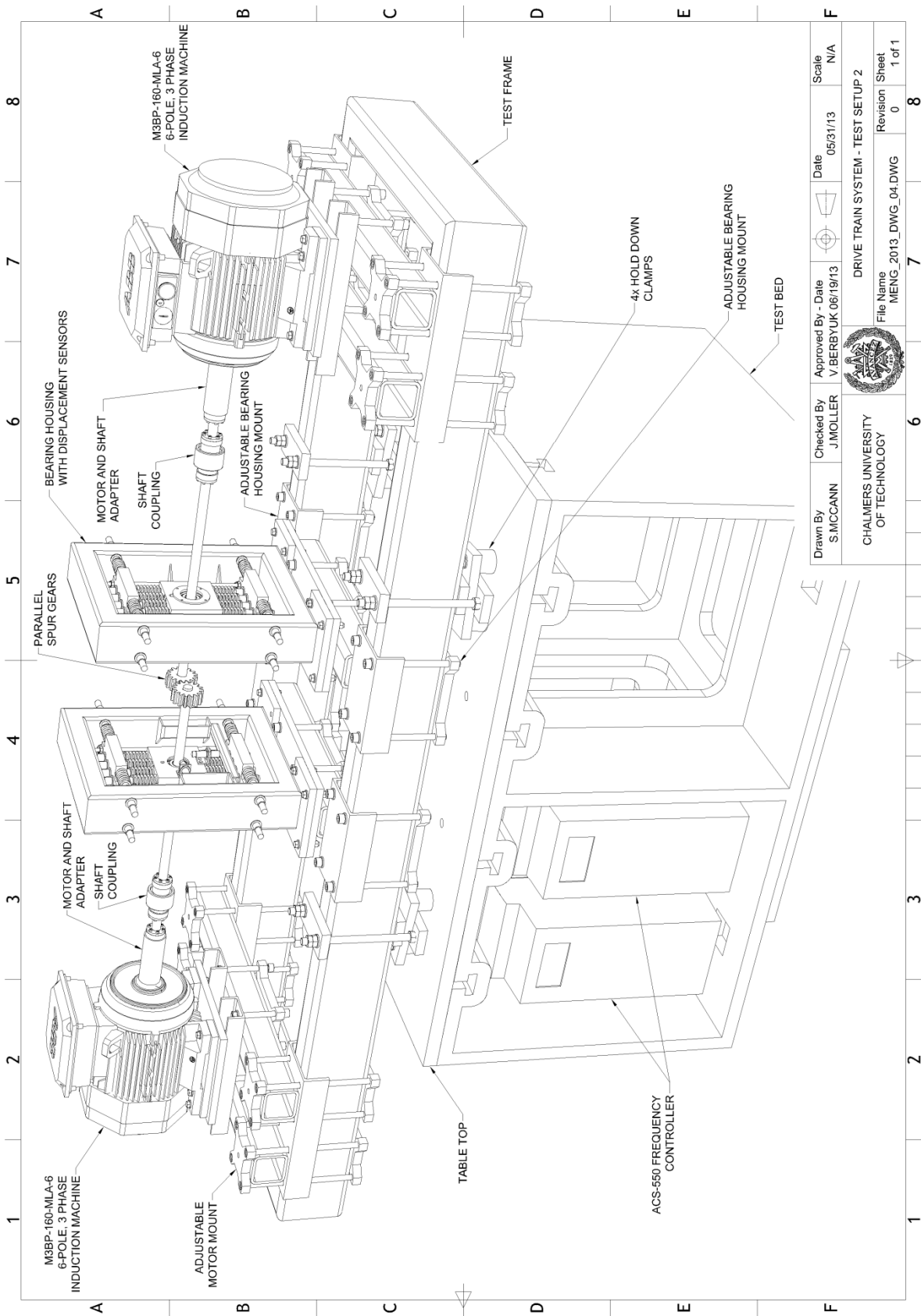
- [12] Carlsson, M, Elofsson, E, et al. *Virtuell design av en testrigg för ett vindkraftverks drivlina*. BSc thesis. Chalmers University of Technology, 2012. Chalmers Reproservice, 2012. Print.
- [13] ABB. *Starting Curves - M3BP 160 MLA 6*. N.p.: ABB, 2013. Print.
- [14] ABB. *Low Voltage Process Performance Motors*. N.p.: ABB, 2011. Web.
- [15] ABB. *Standard Drives - ASC550*. N.p.: ABB, 2009. Print.
- [16] National Instruments. N.p.: National Instruments, n.d. *NI CompactDAQ 8-Slot USB Chassis*. National Instruments, 2012. Web. 12 June 2013.
- [17] "Die Springs." *The Spring Catalogue*. Lesjöfors - European Springs & Pressings. Web. 16 May 2013.  
<[http://catalog.lesjoforsab.com/pdf/en/chapters/59-69\\_EN.pdf](http://catalog.lesjoforsab.com/pdf/en/chapters/59-69_EN.pdf)>.
- [18] Martin, J. W. *Materials for Engineering*. Cambridge: Woodhead Pub., 2006. 169. Print.
- [19] Qi, HJ, K. Joyce, and MC Boyce. "Durometer Hardness and the Stress-strain Behaviour of Elastomeric Materials." *Rubber Chemistry and Technology* 72.2 (2003): 419-35. Web.

## Appendix I - Drawings

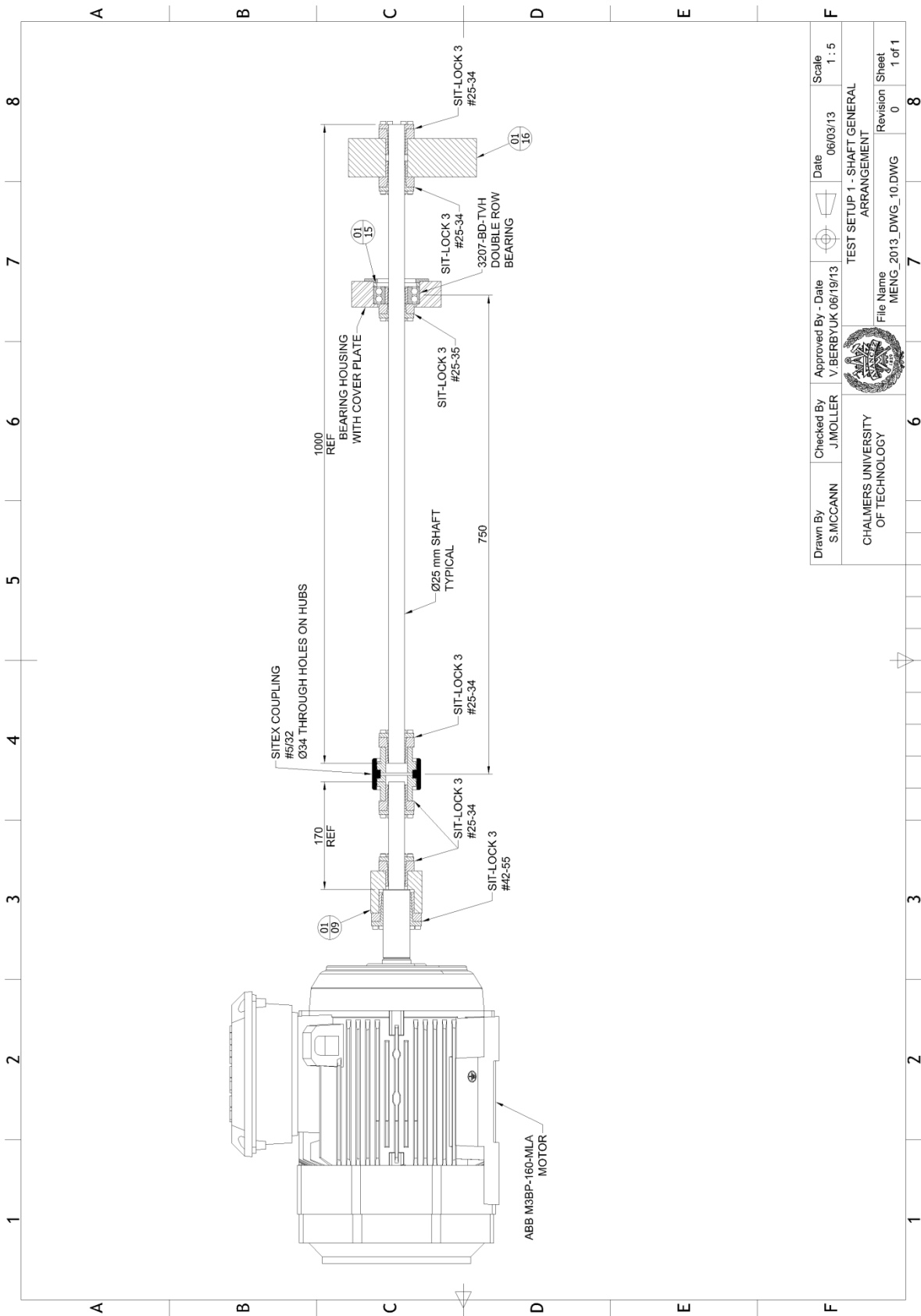
Number	Description	File Name
01	Drive Train System – Test Setup 1	MENG_2013_DWG_03
02	Drive Train System – Test Setup 2	MENG_2013_DWG_04
03	Test Setup 1 – Shaft General Arrangement	MENG_2013_DWG_10
04	Sensor and Cable Identification	MENG_2013_DWG_18
05	3-Phase Schematic	MENG_2013_DWG_37



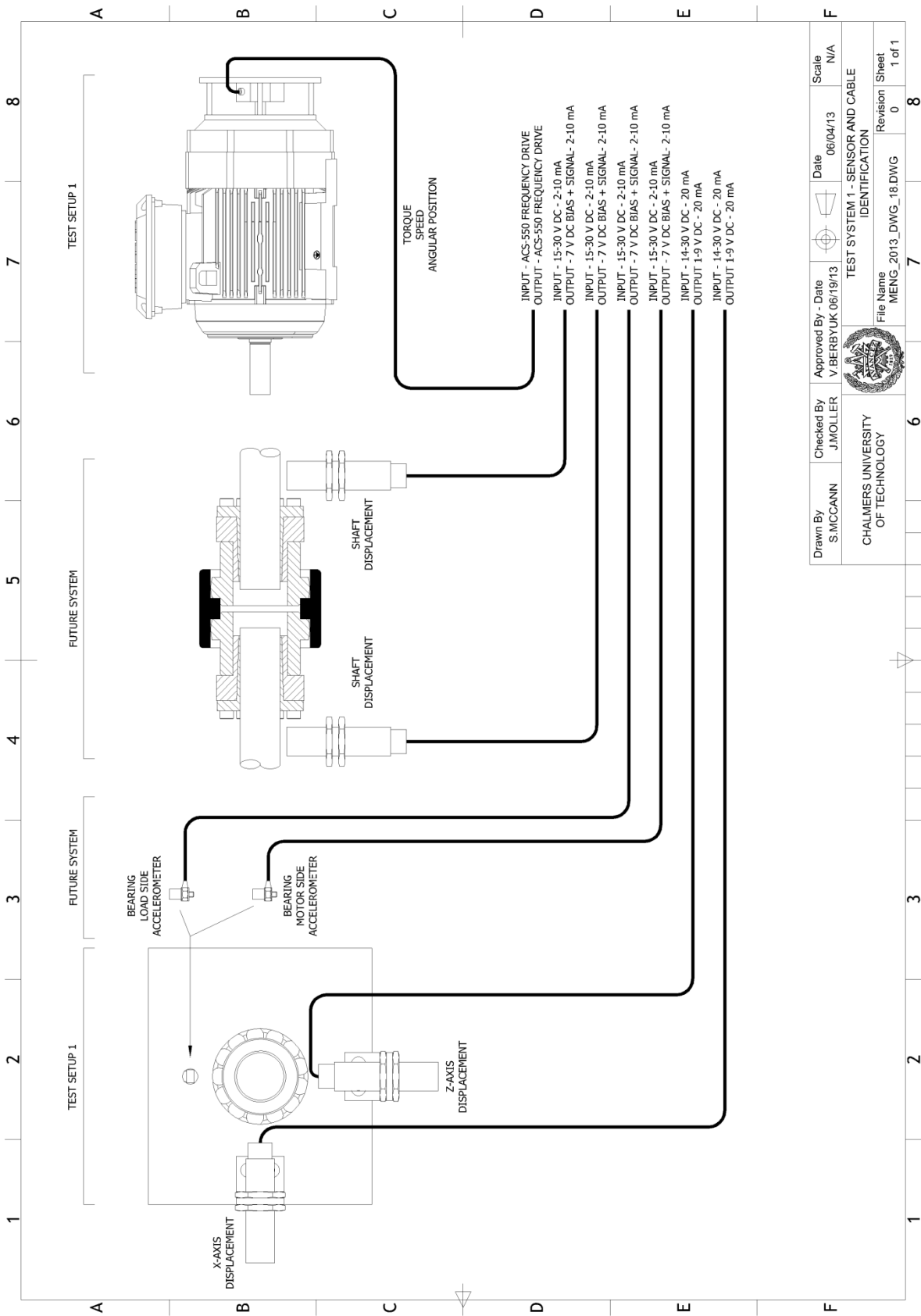
Drawn By S.MCCANN	Checked By J.MOLLER	Approved By - Date V.BERBYUK 06/19/13	Date 05/31/13	Scale N/A
				
DRIVE TRAIN SYSTEM - TEST SETUP 1				
CHALMERS UNIVERSITY OF TECHNOLOGY			File Name MENG_2013_DWG_03.DWG	Revision Sheet 0 1 of 1

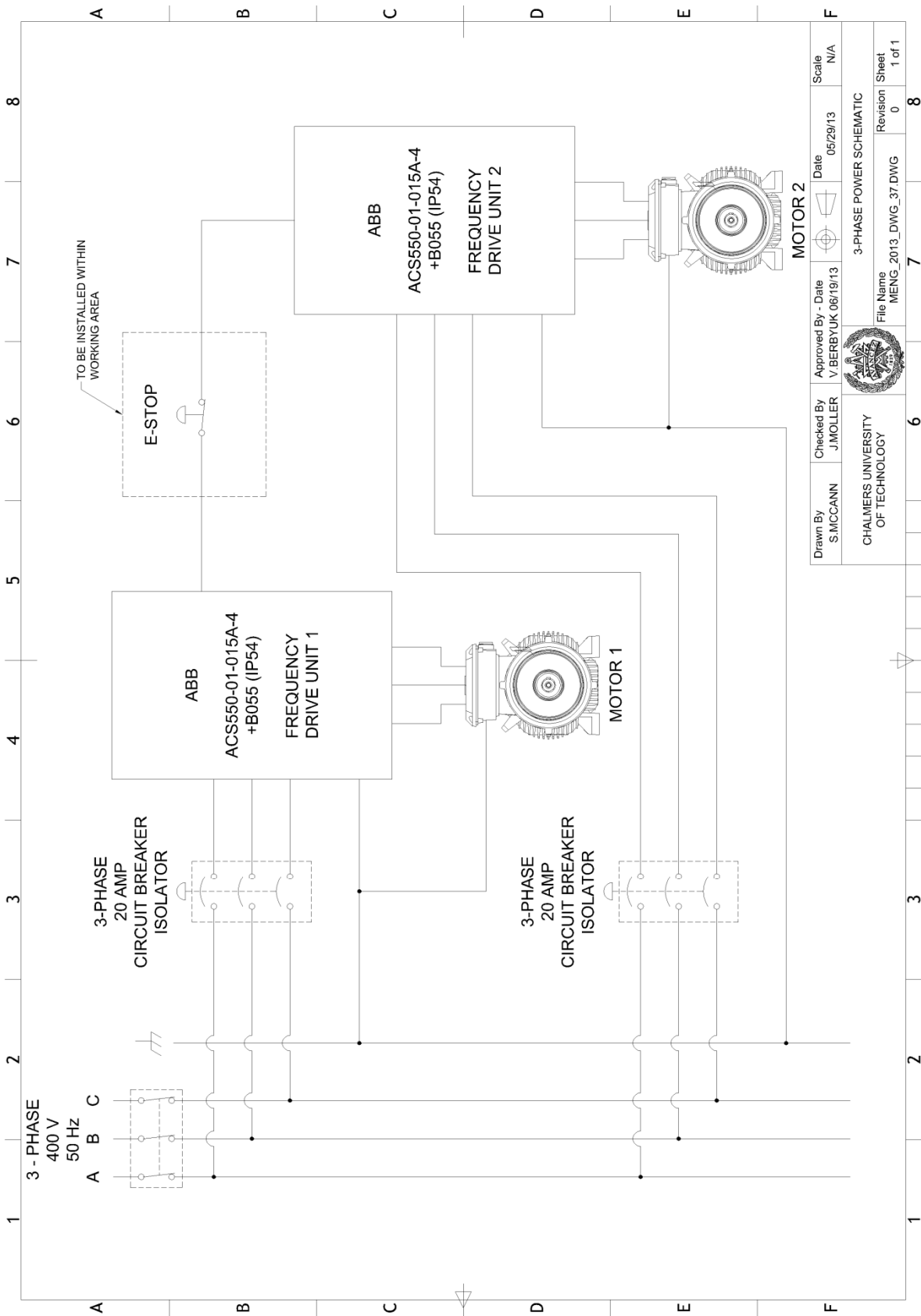


Drawn By	Checked By	Approved By - Date	Date	Scale
S.MCCANN	J.MOLLER	V.BERBYUK 06/19/13	05/31/13	N/A
				
CHALMERS UNIVERSITY OF TECHNOLOGY				
DRIVE TRAIN SYSTEM - TEST SETUP 2				
File Name MENG_2013_DWG_04.DWG			Revision 0	Sheet 1 of 1



Drawn By S.MCCANN	Checked By J.MOLLER	Approved By - Date V.BERBYUK 06/19/13	Date 06/03/13	Scale 1 : 5
				
TEST SETUP 1 - SHAFT GENERAL ARRANGEMENT				
CHALMERS UNIVERSITY OF TECHNOLOGY File Name MENG_2013_DWG_10.DWG				Revision Sheet 0 1 of 1





Drawn By S.MCCANN	Checked By J.MOLLER	Approved By - Date V.BERBY/UK 06/19/13	Date 06/29/13	Scale N/A
 CHALMERS UNIVERSITY OF TECHNOLOGY			3-PHASE POWER SCHEMATIC Revision Sheet MENG_2013_DWG_37.DWG 0 1 of 1	